

Improved model-independent determination of the strong-phase difference between D^0 and $\bar{D}^0 \rightarrow K_{S,L}^0 K^+ K^-$ decays

M. Ablikim¹, M. N. Achasov^{10,c}, P. Adlarson⁶⁴, S. Ahmed¹⁵, M. Albrecht⁴, R. Aliberti²⁸, A. Amoroso^{63A,63C}, Q. An^{60,48}, Anita²¹, X. H. Bai⁵⁴, Y. Bai⁴⁷, O. Bakina²⁹, R. Baldini Ferroli^{23A}, I. Balossino^{24A}, Y. Ban^{38,k}, K. Begzsuren²⁶, J. V. Bennett⁵, N. Berger²⁸, M. Bertani^{23A}, D. Bettoni^{24A}, F. Bianchi^{63A,63C}, J. Biernat⁶⁴, J. Bloms⁵⁷, A. Bortone^{63A,63C}, I. Boyko²⁹, R. A. Briere⁵, H. Cai⁶⁵, X. Cai^{1,48}, A. Calcaterra^{23A}, G. F. Cao^{1,52}, N. Cao^{1,52}, S. A. Cetin^{51B}, J. F. Chang^{1,48}, W. L. Chang^{1,52}, G. Chelkov^{29,b}, D. Y. Chen⁶, G. Chen¹, H. S. Chen^{1,52}, M. L. Chen^{1,48}, S. J. Chen³⁶, X. R. Chen²⁵, Y. B. Chen^{1,48}, Z. J. Chen^{20,l}, W. S. Cheng^{63C}, G. Cibinetto^{24A}, F. Cossio^{63C}, X. F. Cui³⁷, H. L. Dai^{1,48}, J. P. Dai^{42,g}, X. C. Dai^{1,52}, A. Dbeysi¹⁵, R. B. de Boer⁴, D. Dedovich²⁹, Z. Y. Deng¹, A. Denig²⁸, I. Denysenko²⁹, M. Destefanis^{63A,63C}, F. De Mori^{63A,63C}, Y. Ding³⁴, C. Dong³⁷, J. Dong^{1,48}, L. Y. Dong^{1,52}, M. Y. Dong^{1,48,52}, S. X. Du⁶⁸, J. Fang^{1,48}, S. S. Fang^{1,52}, Y. Fang¹, R. Farinelli^{24A}, L. Fava^{63B,63C}, F. Feldbauer⁴, G. Felici^{23A}, C. Q. Feng^{60,48}, M. Fritsch⁴, C. D. Fu¹, Y. Fu¹, X. L. Gao^{60,48}, Y. Gao⁶¹, Y. Gao^{38,k}, Y. G. Gao⁶, I. Garzia^{24A,24B}, E. M. Gersabeck⁵⁵, A. Gilman⁵⁶, K. Goetzen¹¹, L. Gong³⁷, W. X. Gong^{1,48}, W. Gradl²⁸, M. Greco^{63A,63C}, L. M. Gu³⁶, M. H. Gu^{1,48}, S. Gu², Y. T. Gu¹³, C. Y. Guan^{1,52}, A. Q. Guo²², L. B. Guo³⁵, R. P. Guo⁴⁰, Y. P. Guo^{9,h}, Y. P. Guo²⁸, A. Guskov²⁹, S. Han⁶⁵, T. T. Han⁴¹, T. Z. Han^{9,h}, X. Q. Hao¹⁶, F. A. Harris⁵³, K. L. He^{1,52}, F. H. Heinsius⁴, C. H. Heinz²⁸, T. Held⁴, Y. K. Heng^{1,48,52}, M. Himmelreich^{11,f}, T. Holtmann⁴, Y. R. Hou⁵², Z. L. Hou¹, H. M. Hu^{1,52}, J. F. Hu^{42,g}, T. Hu^{1,48,52}, Y. Hu¹, G. S. Huang^{60,48}, L. Q. Huang⁶¹, X. T. Huang⁴¹, Y. P. Huang¹, Z. Huang^{38,k}, N. Huesken⁵⁷, T. Hussain⁶², W. Ikegami Andersson⁶⁴, W. Imoehl²², M. Irshad^{60,48}, S. Jaeger⁴, S. Janchiv^{26,j}, Q. Ji¹, Q. P. Ji¹⁶, X. B. Ji^{1,52}, X. L. Ji^{1,48}, H. B. Jiang⁴¹, X. S. Jiang^{1,48,52}, X. Y. Jiang³⁷, J. B. Jiao⁴¹, Z. Jiao¹⁸, S. Jin³⁶, Y. Jin⁵⁴, T. Johansson⁶⁴, N. Kalantar-Nayestanaki³¹, X. S. Kang³⁴, R. Kappert³¹, M. Kavatsyuk³¹, B. C. Ke^{43,1}, I. K. Keshk⁴, A. Khoukaz⁵⁷, P. Kiese²⁸, R. Kiuchi¹, R. Kliemt¹¹, L. Koch³⁰, O. B. Kolcu^{51B,e}, B. Kopf⁴, M. Kuemmel⁴, M. Kuessner⁴, A. Kupsc⁶⁴, M. G. Kurth^{1,52}, W. Kühn³⁰, J. J. Lane⁵⁵, J. S. Lange³⁰, P. Larin¹⁵, L. Lavezzi^{63C}, H. Leithoff²⁸, M. Lellmann²⁸, T. Lenz²⁸, C. Li³⁹, C. H. Li³³, Cheng Li^{60,48}, D. M. Li⁶⁸, F. Li^{1,48}, G. Li¹, H. B. Li^{1,52}, H. J. Li^{9,h}, J. L. Li⁴¹, J. Q. Li⁴, Ke Li¹, L. K. Li¹, Lei Li³, P. L. Li^{60,48}, P. R. Li³², S. Y. Li⁵⁰, W. D. Li^{1,52}, W. G. Li¹, X. H. Li^{60,48}, X. L. Li⁴¹, Z. B. Li⁴⁹, Z. Y. Li⁴⁹, H. Liang^{60,48}, H. Liang^{1,52}, Y. F. Liang⁴⁵, Y. T. Liang²⁵, L. Z. Liao^{1,52}, J. Libby²¹, C. X. Lin⁴⁹, B. Liu^{42,g}, B. J. Liu¹, C. X. Liu¹, D. Liu^{60,48}, D. Y. Liu^{42,g}, F. H. Liu⁴⁴, Fang Liu¹, Feng Liu⁶, H. B. Liu¹³, H. M. Liu^{1,52}, Huanhuan Liu¹, Huihui Liu¹⁷, J. B. Liu^{60,48}, J. Y. Liu^{1,52}, K. Liu¹, K. Y. Liu³⁴, Ke Liu⁶, L. Liu^{60,48}, Q. Liu⁵², S. B. Liu^{60,48}, Shuai Liu⁴⁶, T. Liu^{1,52}, X. Liu³², Y. B. Liu³⁷, Z. A. Liu^{1,48,52}, Z. Q. Liu⁴¹, Y. F. Long^{38,k}, X. C. Lou^{1,48,52}, F. X. Lu¹⁶, H. J. Lu¹⁸, J. D. Lu^{1,52}, J. G. Lu^{1,48}, X. L. Lu¹, Y. Lu¹, Y. P. Lu^{1,48}, C. L. Luo³⁵, M. X. Luo⁶⁷, P. W. Luo⁴⁹, T. Luo^{9,h}, X. L. Luo^{1,48}, S. Lusso^{63C}, X. R. Lyu⁵², F. C. Ma³⁴, H. L. Ma¹, L. L. Ma⁴¹, M. M. Ma^{1,52}, Q. M. Ma¹, R. Q. Ma^{1,52}, R. T. Ma⁵², X. N. Ma³⁷, X. X. Ma^{1,52}, X. Y. Ma^{1,48}, Y. M. Ma⁴¹, F. E. Maas¹⁵, M. Maggiora^{63A,63C}, S. Maldaner²⁸, S. Malde⁵⁸, Q. A. Malik⁶², A. Mangoni^{23B}, Y. J. Mao^{38,k}, Z. P. Mao¹, S. Marcello^{63A,63C}, Z. X. Meng⁵⁴, J. G. Messchendorp³¹, G. Mezzadri^{24A}, T. J. Min³⁶, R. E. Mitchell²², X. H. Mo^{1,48,52}, Y. J. Mo⁶, N. Yu. Muchnoi^{10,c}, H. Muramatsu⁵⁶, S. Nakhoul^{11,f}, Y. Nefedov²⁹, F. Nerling^{11,f}, I. B. Nikolaev^{10,c}, Z. Ning^{1,48}, S. Nisar^{8,i}, S. L. Olsen⁵², Q. Ouyang^{1,48,52}, S. Pacetti^{23B,23C}, X. Pan^{9,h}, Y. Pan⁵⁵, A. Pathak¹, P. Patteri^{23A}, M. Pelizaeus⁴, H. P. Peng^{60,48}, K. Peters^{11,f}, J. Pettersson⁶⁴, J. L. Ping³⁵, R. G. Ping^{1,52}, A. Pitka⁴, R. Poling⁵⁶, V. Prasad^{60,48}, H. Qi^{60,48}, H. R. Qi⁵⁰, M. Qi³⁶, T. Y. Qi⁹, T. Y. Qi², S. Qian^{1,48}, W.-B. Qian⁵², Z. Qian⁴⁹, C. F. Qiao⁵², L. Q. Qin¹², X. S. Qin⁴, Z. H. Qin^{1,48}, J. F. Qiu¹, S. Q. Qu³⁷, K. H. Rashid⁶², K. Ravindran²¹, C. F. Redmer²⁸, A. Rivetti^{63C}, V. Rodin³¹, M. Rolo^{63C}, G. Rong^{1,52}, Ch. Rosner¹⁵, M. Rump⁵⁷, A. Sarantsev^{29,d}, Y. Schelhaas²⁸, C. Schnier⁴, K. Schoenning⁶⁴, M. Scodeggio^{24A}, D. C. Shan⁴⁶, W. Shan¹⁹, X. Y. Shan^{60,48}, M. Shao^{60,48}, C. P. Shen⁹, P. X. Shen³⁷, X. Y. Shen^{1,52}, H. C. Shi^{60,48}, R. S. Shi^{1,52}, X. Shi^{1,48}, X. D. Shi^{60,48}, J. J. Song⁴¹, Q. Q. Song^{60,48}, W. M. Song^{27,1}, Y. X. Song^{38,k}, S. Sosio^{63A,63C}, S. Spataro^{63A,63C}, F. F. Sui⁴¹, G. X. Sun¹, J. F. Sun¹⁶, L. Sun⁶⁵, S. S. Sun^{1,52}, T. Sun^{1,52}, W. Y. Sun³⁵, X. Sun^{20,l}, Y. J. Sun^{60,48}, Y. K. Sun^{60,48}, Y. Z. Sun¹, Z. T. Sun¹, Y. H. Tan⁶⁵, Y. X. Tan^{60,48}, C. J. Tang⁴⁵, G. Y. Tang¹, J. Tang⁴⁹, V. Thoren⁶⁴, B. Tsednee²⁶, I. Uman^{51D}, B. Wang¹, B. L. Wang⁵², C. W. Wang³⁶, D. Y. Wang^{38,k}, H. P. Wang^{1,52}, K. Wang^{1,48}, L. L. Wang¹, M. Wang⁴¹, M. Z. Wang^{38,k}, Meng Wang^{1,52}, W. H. Wang⁶⁵, W. P. Wang^{60,48}, X. Wang^{38,k}, X. F. Wang³², X. L. Wang^{9,h}, Y. Wang⁴⁹, Y. Wang^{60,48}, Y. D. Wang¹⁵, Y. F. Wang^{1,48,52}, Y. Q. Wang¹, Z. Wang^{1,48}, Z. Y. Wang¹, Ziyi Wang⁵², Zongyuan Wang^{1,52}, D. H. Wei¹², P. Weidenkaff²⁸, F. Weidner⁵⁷, S. P. Wen¹, D. J. White⁵⁵, U. Wiedner⁴, G. Wilkinson⁵⁸, M. Wolke⁶⁴, L. Wollenberg⁴, J. F. Wu^{1,52}, L. H. Wu¹, L. J. Wu^{1,52}, X. Wu^{9,h}, Z. Wu^{1,48}, L. Xia^{60,48}, H. Xiao^{9,h}, S. Y. Xiao¹, Y. J. Xiao^{1,52}, Z. J. Xiao³⁵, X. H. Xie^{38,k}, Y. G. Xie^{1,48}, Y. H. Xie⁶, T. Y. Xing^{1,52}, X. A. Xiong^{1,52}, G. F. Xu¹, J. J. Xu³⁶, Q. J. Xu¹⁴, W. Xu^{1,52}, X. P. Xu⁴⁶, F. Yan^{9,h}, L. Yan^{63A,63C}, L. Yan^{9,h}, W. B. Yan^{60,48}, W. C. Yan⁶⁸, Xu Yan⁴⁶, H. J. Yang^{42,g}, H. X. Yang¹, L. Yang⁶⁵, R. X. Yang^{60,48}, S. L. Yang^{1,52}, Y. H. Yang³⁶, Y. X. Yang¹², Yifan Yang^{1,52}, Zhi Yang²⁵, M. Ye^{1,48}, M. H. Ye⁷, J. H. Yin¹, Z. Y. You⁴⁹, B. X. Yu^{1,48,52}, C. X. Yu³⁷, G. Yu^{1,52}, J. S. Yu^{20,l}, T. Yu⁶¹, C. Z. Yuan^{1,52}, W. Yuan^{63A,63C}, X. Q. Yuan^{38,k}, Y. Yuan¹, Z. Y. Yuan⁴⁹, C. X. Yue³³, A. Yuncu^{51B,a}, A. A. Zafar⁶², Y. Zeng^{20,l}, B. X. Zhang¹, Guangyi Zhang¹⁶, H. H. Zhang⁴⁹, H. Y. Zhang^{1,48}, J. L. Zhang⁶⁶, J. Q. Zhang⁴, J. W. Zhang^{1,48,52}, J. Y. Zhang¹, J. Z. Zhang^{1,52}, Jiayu Zhang^{1,52}, Jiawei Zhang^{1,52}, L. Zhang¹, Lei Zhang³⁶, S. Zhang⁴⁹, S. F. Zhang³⁶, T. J. Zhang^{42,g}, X. Y. Zhang⁴¹, Y. Zhang⁵⁸, Y. H. Zhang^{1,48}, Y. T. Zhang^{60,48}, Yan Zhang^{60,48}, Yao Zhang¹, Yi Zhang^{9,h}, Z. H. Zhang⁶, Z. Y. Zhang⁶⁵, G. Zhao¹, J. Zhao³³, J. Y. Zhao^{1,52}, J. Z. Zhao^{1,48}, Lei Zhao^{60,48}, Ling Zhao¹, M. G. Zhao³⁷, Q. Zhao¹, S. J. Zhao⁶⁸, Y. B. Zhao^{1,48}, Y. X. Zhao²⁵, Z. G. Zhao^{60,48}, A. Zhemchugov^{29,b}, B. Zheng⁶¹, J. P. Zheng^{1,48}, Y. Zheng^{38,k}, Y. H. Zheng⁵², B. Zhong³⁵, C. Zhong⁶¹, L. P. Zhou^{1,52}, Q. Zhou^{1,52}, X. Zhou⁶⁵, X. K. Zhou⁵², X. R. Zhou^{60,48}, A. N. Zhu^{1,52}, J. Zhu³⁷, K. Zhu¹, K. J. Zhu^{1,48,52}, S. H. Zhu⁵⁹, W. J. Zhu³⁷, X. L. Zhu⁵⁰, Y. C. Zhu^{60,48}, Z. A. Zhu^{1,52}, B. S. Zou¹, J. H. Zou¹

(BESIII Collaboration)

¹ Institute of High Energy Physics, Beijing 100049, People's Republic of China² Beihang University, Beijing 100191, People's Republic of China³ Beijing Institute of Petrochemical Technology, Beijing 102617, People's Republic of China⁴ Bochum Ruhr-University, D-44780 Bochum, Germany⁵ Carnegie Mellon University, Pittsburgh, Pennsylvania 15213, USA

- ⁶ *Central China Normal University, Wuhan 430079, People's Republic of China*
- ⁷ *China Center of Advanced Science and Technology, Beijing 100190, People's Republic of China*
- ⁸ *COMSATS University Islamabad, Lahore Campus, Defence Road, Off Raiwind Road, 54000 Lahore, Pakistan*
- ⁹ *Fudan University, Shanghai 200443, People's Republic of China*
- ¹⁰ *G.I. Budker Institute of Nuclear Physics SB RAS (BINP), Novosibirsk 630090, Russia*
- ¹¹ *GSI Helmholtzcentre for Heavy Ion Research GmbH, D-64291 Darmstadt, Germany*
- ¹² *Guangxi Normal University, Guilin 541004, People's Republic of China*
- ¹³ *Guangxi University, Nanning 530004, People's Republic of China*
- ¹⁴ *Hangzhou Normal University, Hangzhou 310036, People's Republic of China*
- ¹⁵ *Helmholtz Institute Mainz, Johann-Joachim-Becher-Weg 45, D-55099 Mainz, Germany*
- ¹⁶ *Henan Normal University, Xinxiang 453007, People's Republic of China*
- ¹⁷ *Henan University of Science and Technology, Luoyang 471003, People's Republic of China*
- ¹⁸ *Huangshan College, Huangshan 245000, People's Republic of China*
- ¹⁹ *Hunan Normal University, Changsha 410081, People's Republic of China*
- ²⁰ *Hunan University, Changsha 410082, People's Republic of China*
- ²¹ *Indian Institute of Technology Madras, Chennai 600036, India*
- ²² *Indiana University, Bloomington, Indiana 47405, USA*
- ²³ (A)*INFN Laboratori Nazionali di Frascati, I-00044, Frascati, Italy; (B)INFN Sezione di Perugia, I-06100, Perugia, Italy; (C)University of Perugia, I-06100, Perugia, Italy*
- ²⁴ (A)*INFN Sezione di Ferrara, I-44122, Ferrara, Italy; (B)University of Ferrara, I-44122, Ferrara, Italy*
- ²⁵ *Institute of Modern Physics, Lanzhou 730000, People's Republic of China*
- ²⁶ *Institute of Physics and Technology, Peace Ave. 54B, Ulaanbaatar 13330, Mongolia*
- ²⁷ *Jilin University, Changchun 130012, People's Republic of China*
- ²⁸ *Johannes Gutenberg University of Mainz, Johann-Joachim-Becher-Weg 45, D-55099 Mainz, Germany*
- ²⁹ *Joint Institute for Nuclear Research, 141980 Dubna, Moscow region, Russia*
- ³⁰ *Justus-Liebig-Universitaet Giessen, II. Physikalisches Institut, Heinrich-Buff-Ring 16, D-35392 Giessen, Germany*
- ³¹ *KVI-CART, University of Groningen, NL-9747 AA Groningen, The Netherlands*
- ³² *Lanzhou University, Lanzhou 730000, People's Republic of China*
- ³³ *Liaoning Normal University, Dalian 116029, People's Republic of China*
- ³⁴ *Liaoning University, Shenyang 110036, People's Republic of China*
- ³⁵ *Nanjing Normal University, Nanjing 210023, People's Republic of China*
- ³⁶ *Nanjing University, Nanjing 210093, People's Republic of China*
- ³⁷ *Nankai University, Tianjin 300071, People's Republic of China*
- ³⁸ *Peking University, Beijing 100871, People's Republic of China*
- ³⁹ *Qufu Normal University, Qufu 273165, People's Republic of China*
- ⁴⁰ *Shandong Normal University, Jinan 250014, People's Republic of China*
- ⁴¹ *Shandong University, Jinan 250100, People's Republic of China*
- ⁴² *Shanghai Jiao Tong University, Shanghai 200240, People's Republic of China*
- ⁴³ *Shanxi Normal University, Linfen 041004, People's Republic of China*
- ⁴⁴ *Shanxi University, Taiyuan 030006, People's Republic of China*
- ⁴⁵ *Sichuan University, Chengdu 610064, People's Republic of China*
- ⁴⁶ *Soochow University, Suzhou 215006, People's Republic of China*
- ⁴⁷ *Southeast University, Nanjing 211100, People's Republic of China*
- ⁴⁸ *State Key Laboratory of Particle Detection and Electronics, Beijing 100049, Hefei 230026, People's Republic of China*
- ⁴⁹ *Sun Yat-Sen University, Guangzhou 510275, People's Republic of China*
- ⁵⁰ *Tsinghua University, Beijing 100084, People's Republic of China*
- ⁵¹ (A)*Ankara University, 06100 Tandogan, Ankara, Turkey; (B)Istanbul Bilgi University, 34060 Eyup, Istanbul, Turkey; (C)Uludag University, 16059 Bursa, Turkey; (D)Near East University, Nicosia, North Cyprus, Mersin 10, Turkey*
- ⁵² *University of Chinese Academy of Sciences, Beijing 100049, People's Republic of China*
- ⁵³ *University of Hawaii, Honolulu, Hawaii 96822, USA*
- ⁵⁴ *University of Jinan, Jinan 250022, People's Republic of China*
- ⁵⁵ *University of Manchester, Oxford Road, Manchester, M13 9PL, United Kingdom*
- ⁵⁶ *University of Minnesota, Minneapolis, Minnesota 55455, USA*
- ⁵⁷ *University of Muenster, Wilhelm-Klemm-Str. 9, 48149 Muenster, Germany*
- ⁵⁸ *University of Oxford, Keble Rd, Oxford, UK OX13RH*
- ⁵⁹ *University of Science and Technology Liaoning, Anshan 114051, People's Republic of China*
- ⁶⁰ *University of Science and Technology of China, Hefei 230026, People's Republic of China*
- ⁶¹ *University of South China, Hengyang 421001, People's Republic of China*
- ⁶² *University of the Punjab, Lahore-54590, Pakistan*
- ⁶³ (A)*University of Turin, I-10125, Turin, Italy; (B)University of Eastern Piedmont, I-15121, Alessandria, Italy; (C)INFN, I-10125, Turin, Italy*
- ⁶⁴ *Uppsala University, Box 516, SE-75120 Uppsala, Sweden*
- ⁶⁵ *Wuhan University, Wuhan 430072, People's Republic of China*
- ⁶⁶ *Xinyang Normal University, Xinyang 464000, People's Republic of China*

⁶⁷ Zhejiang University, Hangzhou 310027, People's Republic of China

⁶⁸ Zhengzhou University, Zhengzhou 450001, People's Republic of China

^a Also at Bogazici University, 34342 Istanbul, Turkey

^b Also at the Moscow Institute of Physics and Technology, Moscow 141700, Russia

^c Also at the Novosibirsk State University, Novosibirsk, 630090, Russia

^d Also at the NRC "Kurchatov Institute", PNPI, 188300, Gatchina, Russia

^e Also at Istanbul Arel University, 34295 Istanbul, Turkey

^f Also at Goethe University Frankfurt, 60323 Frankfurt am Main, Germany

^g Also at Key Laboratory for Particle Physics, Astrophysics and Cosmology, Ministry of Education; Shanghai Key Laboratory for Particle Physics and Cosmology; Institute of Nuclear and Particle Physics, Shanghai 200240, People's Republic of China

^h Also at Key Laboratory of Nuclear Physics and Ion-beam Application (MOE) and Institute of Modern Physics, Fudan University, Shanghai 200443, People's Republic of China

ⁱ Also at Harvard University, Department of Physics, Cambridge, MA, 02138, USA

^j Currently at: Institute of Physics and Technology, Peace Ave.54B, Ulaanbaatar 13330, Mongolia

^k Also at State Key Laboratory of Nuclear Physics and Technology, Peking University, Beijing 100871, People's Republic of China

^l School of Physics and Electronics, Hunan University, Changsha 410082, China

We present a measurement of the strong-phase difference between D^0 and $\bar{D}^0 \rightarrow K_{S,L}^0 K^+ K^-$ decays, performed through a study of quantum-entangled pairs of charm mesons. The measurement exploits a data sample equivalent to an integrated luminosity of 2.93 fb^{-1} , collected by the BESIII detector in e^+e^- collisions corresponding to the mass of the $\psi(3770)$ resonance. The strong-phase difference is an essential input to the determination of the Cabibbo-Kobayashi-Maskawa (CKM) angle γ/ϕ_3 through the decay $B^- \rightarrow DK^-$, where D can be either a D^0 or a \bar{D}^0 decaying to $K_{S,L}^0 K^+ K^-$. This is the most precise measurement to date of the strong-phase difference in these decays.

I. INTRODUCTION

In the Standard Model (SM), the charged-weak interaction in the quark sector is described by the Cabibbo-Kobayashi-Maskawa matrix (CKM) [1]. One of the primary goals of flavor physics experiments is to determine the angles α, β and γ (or ϕ_2, ϕ_1 and ϕ_3) of the $b-d$ CKM unitary triangle precisely. Currently, the most precise measurements of γ are extracted using tree-level $B^- \rightarrow DK^-$ decays [2]. Here and elsewhere in this paper D refers to either a D^0 or a \bar{D}^0 meson decaying into the same final state and charge conjugation is implicit, unless stated otherwise. The sensitivity to γ arises from the interference of two amplitudes: $b \rightarrow \bar{c}us$ that results in the $B^- \rightarrow D^0 K^-$ decay, and $b \rightarrow u\bar{c}s$ that leads to the $B^- \rightarrow \bar{D}^0 K^-$ decay. The latter amplitude is both CKM- and color-suppressed relative to the former. The value of γ measured with such tree-level transitions is insensitive to loop-level contributions [3]. Therefore, tests for new physics that are made by comparing unitarity triangle parameters measured using tree and loop processes can be improved by more precise determinations of γ [4, 5].

Different methods of determining γ are classified based upon the decay products of the D decay: CP eigenstates (GLW method) [2], flavor-eigenstates (ADS method) [6], and self-conjugate multibody states (BPGGSZ method) [7–9]. The most widely used D decays for the BPGGSZ method are $D \rightarrow K_S^0 h^+ h^-$, where $h = \pi, K$. Measurements of γ using these final states have been performed by the Belle, BaBar and LHCb Collaborations [9–11]. Recently the first constraints on γ using the BPGGSZ method with a four-body D decay were reported [12]. BPGGSZ analyses require an understanding of the interference effects between D^0 and \bar{D}^0 decays, especially concerning the strong-phase difference between the D^0 and \bar{D}^0 decay amplitudes.

A precise measurement of the strong-phase difference in $D \rightarrow K_{S,L}^0 \pi^+ \pi^-$ decays was reported by the BESIII Collaboration recently [13]. The first measurements of the strong-phase difference between D^0 and \bar{D}^0 decaying to the $K_{S,L}^0 K^+ K^-$ final state were reported by the CLEO Collaboration, using a data set equivalent to an integrated luminosity of 818 pb^{-1} that was collected at a center-of-mass energy corresponding to the mass of the $\psi(3770)$ resonance [14]. In this paper, we present an improved measurement of the strong-phase parameters for $D \rightarrow K_{S,L}^0 K^+ K^-$ decays, using a $\psi(3770)$ data sample corresponding to an integrated luminosity of 2.93 fb^{-1} recorded by the BESIII detector. This measurement can be used as an input to the model-independent measurement of γ using the BPGGSZ method. Moreover, these strong-phase parameters serve as an essential input to the model-independent determination of charm-mixing parameters and in probing CP violation with $D \rightarrow K_{S,L}^0 K^+ K^-$ decays [15].

The $D \rightarrow K_S^0 K^+ K^-$ decay proceeds via various intermediate resonances, which leads to a significant strong-phase variation over the phase space. We define the kinematic variables $m_{\pm}^2 = (P_{K_S^0} + P_{K_{\pm}})^2$, which serve as the basis of the $D \rightarrow K_S^0 K^+ K^-$ Dalitz plot. Here, P_i ($i = K_S^0, K^+, K^-$) is the four-momentum of the D decay product. The amplitude for $B^- \rightarrow D(K_S^0 K^+ K^-) K^-$ at (m_+^2, m_-^2) can be written as

$$f_{B^-}(m_+^2, m_-^2) \propto f_D(m_+^2, m_-^2) + r_B e^{i(\delta_B - \gamma)} f_{\bar{D}}(m_+^2, m_-^2), \quad (1)$$

where r_B is the ratio of the magnitude of the suppressed to the favored B -decay amplitude, δ_B is the CP -conserving strong-phase difference between favored and suppressed B -decay amplitudes, γ is the weak-phase difference between the B decay amplitudes, and $f_D(m_+^2, m_-^2)$ ($f_{\bar{D}}(m_+^2, m_-^2)$) is the am-

plitude of the $D^0 \rightarrow K_S^0 K^+ K^-$ ($\bar{D}^0 \rightarrow K_S^0 K^+ K^-$) decay. We neglect CP violation in D decays as in Ref. [8], and can thus use the relation $f_{\bar{D}}(m_+^2, m_-^2) = f_D(m_-^2, m_+^2)$ so that Eq. (1) can be written as

$$f_{B^-}(m_+^2, m_-^2) \propto f_D(m_+^2, m_-^2) + r_B e^{i(\delta_B - \gamma)} f_D(m_-^2, m_+^2). \quad (2)$$

$$\Gamma_{B^-}(m_+^2, m_-^2) \propto |f_D(m_+^2, m_-^2)|^2 + r_B^2 |f_D(m_-^2, m_+^2)|^2 + 2r_B |f_D(m_+^2, m_-^2)| |f_D(m_-^2, m_+^2)| \cos(\Delta\delta_D + \delta_B - \gamma), \quad (3)$$

where $\Delta\delta_D \equiv \delta_D(m_+^2, m_-^2) - \delta_D(m_-^2, m_+^2)$, and $\delta_D(m_+^2, m_-^2)$ is the strong phase of $f_D(m_+^2, m_-^2)$. Hence, knowledge of $\Delta\delta_D$ is essential for the determination of γ in $B^- \rightarrow DK^-$ decays.

In the literature, both model-dependent and model-independent BPGGSZ methods are used. In the model-dependent approach, the D^0 amplitude is obtained using a flavor-tagged D^0 meson sample selected from the $D^{*\pm} \rightarrow D^0(K_S^0 K^+ K^-)\pi^\pm$ decay, which is fit to an amplitude model describing the decay of $D^0 \rightarrow K_S^0 K^+ K^-$ [16] to determine $f_D(m_+^2, m_-^2)$. The amplitude model is then used in an unbinned likelihood fit to the B -meson data sample to determine γ , δ_B , and r_B . However, this method results in a model-dependent systematic uncertainty on the measured value of γ which is difficult to quantify [17]. These model-dependent uncertainties have been estimated to lie between 3° to 9° [18, 19], which limits the precision on γ that future measurements performed with much larger B -meson data samples [20, 21] can obtain.

An alternative method of measuring γ is in a model-independent manner that relies on defining a number of bins in the $D^0 \rightarrow K_S^0 K^+ K^-$ Dalitz plot [8]. This approach determines γ from the measured rate in each bin of the Dalitz plot, rather than fitting the Dalitz plot distribution to an amplitude model. The method requires information about $\Delta\delta_D(m_+^2, m_-^2)$ in each bin, which is accessible at the $\psi(3770)$ resonance by exploiting the quantum coherence of the $D^0 \bar{D}^0$ pair produced in $\psi(3770)$ decays. The advantage of this method is that the hard-to-quantify systematic uncertainty related to the model assumption is replaced by the uncertainty on the binned strong-phase parameters of the D decay mode. These strong-phase parameter uncertainties are statistically dominated, and thus well understood. The major disadvantage of the model-independent method is the inevitable loss of information that arises from binning, which reduces the statistical sensitivity of the γ measurement by approximately 80% compared to the model-dependent method [14].

The remainder of this paper is structured as follows. In Sec. II we define the formalism used to measure the strong-phase parameters with $\psi(3770)$ data. We explain the Dalitz-plot binning in Sec. III. In Sec. IV we outline the features of the BESIII detector and the simulation techniques used in the analysis. We describe the event-selection criteria and the procedure for estimating the data yields in Secs. V and VI,

Therefore, the decay rate of a B^- meson is

respectively. In Sec. VII we explain the procedure for estimating the bin yields, including the various corrections applied. We describe the extraction of strong-phase parameters and the calculation of systematic uncertainties in Secs. VIII and IX, respectively. We present a discussion on the impact of these results on γ in Sec. X. In Sec. XI we give the conclusion and outlook.

II. FORMALISM

The model-independent method [8] for a three-body D decay is implemented as follows. The entire Dalitz plot is divided into $2\mathcal{N}$ bins, with \mathcal{N} bins symmetrically placed on either side of the $m_+^2 = m_-^2$ line. We follow the convention in which bins with $m_+^2 \geq m_-^2$ are labelled with i and bins with $m_+^2 < m_-^2$ are labelled with $-i$. Thus, the $2\mathcal{N}$ bins are assigned labels from $-\mathcal{N}$ to \mathcal{N} excluding zero. The interchange of the Dalitz plot variables $m_+^2 \leftrightarrow m_-^2$ corresponds to the interchange of positions of the bins $i \leftrightarrow -i$. In order to extract the strong-phase difference parameters, we need to determine the yield in each bin for flavor-, CP - and mixed- CP tagged $D \rightarrow K_S^0 K^+ K^-$ decays. The number of flavor-tagged $D^0 \rightarrow K_S^0 K^+ K^-$ decays K_i in the i th bin of the Dalitz plot is defined as

$$K_i = a_D \int_i |f_D(m_+^2, m_-^2)|^2 dm_+^2 dm_-^2 = a_D F_i, \quad (4)$$

where a_D is a normalization factor equal to the total number of $D^0 \rightarrow K_S^0 K^+ K^-$ decays in the flavor-tagged charm sample, F_i is the fraction of $D^0 \rightarrow K_S^0 K^+ K^-$ decays in the i th bin, and the integral is over the (m_+^2, m_-^2) region defined by the i th bin. Here and elsewhere the values of $K_{(-)i}$ are corrected for efficiency and also for the presence of any doubly Cabibbo-suppressed (DCS) component (see Sec. VII A). We assume $f_D(m_+^2, m_-^2)$ has been normalized such that

$$\int |f_D(m_+^2, m_-^2)|^2 dm_+^2 dm_-^2 = 1, \quad (5)$$

where the integral is over the whole Dalitz plot. For each bin the interference between D^0 and \bar{D}^0 decays can be parameterized by two variables c_i and s_i , which are the amplitude-

weighted averages of $\cos \Delta\delta_D$ and $\sin \Delta\delta_D$, defined as:

$$c_i \equiv \frac{1}{\sqrt{F_i F_{-i}}} \int_i |f_D(m_+^2, m_-^2)| |f_D(m_-^2, m_+^2)| \times \cos[\Delta\delta_D(m_+^2, m_-^2)] dm_+^2 dm_-^2, \quad (6)$$

and

$$s_i \equiv \frac{1}{\sqrt{F_i F_{-i}}} \int_i |f_D(m_+^2, m_-^2)| |f_D(m_-^2, m_+^2)| \times \sin[\Delta\delta_D(m_+^2, m_-^2)] dm_+^2 dm_-^2. \quad (7)$$

From Eqs. (6) and (7) it is evident that $c_i = c_{-i}$, $s_i = -s_{-i}$ and $c_i^2 + s_i^2 \leq 1$. The equality is satisfied only if f_D is constant throughout the bin. Thus the yield of B^\pm decays in the i th bin, N_i^\mp , is obtained by integrating Eq. (3), which results in

$$N_i^\mp \propto K_{\pm i} + r_B^2 K_{\mp i} + 2\sqrt{K_i K_{-i}} (x_{B\mp} \cdot c_i + y_{B\mp} \cdot s_i), \quad (8)$$

where $x_{B\mp} \equiv r_B \cos(\delta_B \mp \gamma)$, $y_{B\mp} \equiv r_B \sin(\delta_B \mp \gamma)$ and $r_B^2 = x_{B\mp}^2 + y_{B\mp}^2$. A maximum likelihood fit to binned $B^- \rightarrow DK^-$ decay yields, using Eq. (8) as a probability density function with externally measured values of c_i and s_i as inputs, then allows γ to be determined along with r_B and δ_B .

We now describe how $\psi(3770)$ data are used to determine the values of c_i and s_i . The $D^0 \bar{D}^0$ pair from the decay of the $\psi(3770)$ (or if directly produced from the virtual photon in an e^+e^- annihilation) is in a C -odd eigenstate, as long as there are no additional particles in the final state. This quantum correlation between the mesons leads to the total $D^0 \bar{D}^0$ decay rate being sensitive to the strong-phase difference between the D^0 and \bar{D}^0 amplitudes. For example, the decay of one D to a CP -even eigenstate fixes the other D to the CP -odd admixture of $(D^0 - \bar{D}^0)/\sqrt{2}$. Hence, if the other D decays to $K_{S,L}^0 K^+ K^-$, the total rate will be sensitive to the interference between the D^0 and \bar{D}^0 amplitudes and the strong-phase parameters. Generally, this interference affects the decays of one

D in combination with the other. If only one D meson is reconstructed, leaving the companion D meson to decay to any final state, the decay rate is largely insensitive to the effects of quantum correlations; we refer to the reconstructed samples of such events as single-tag (ST) decays. If both D mesons are required to be in specific final states, the rates can be significantly enhanced or suppressed in the quantum-correlated events compared to the expected rate if the decays are uncorrelated; we refer to the reconstructed samples of such events as double-tag (DT) decays. Hereafter, all the D decay final states, except the signal mode $K_{S,L}^0 K^+ K^-$, are referred to as ‘‘tags’’.

The $D \rightarrow K_S^0 K^+ K^-$ decay amplitude from a CP eigenstate is

$$f_\pm(m_+^2, m_-^2) = \frac{1}{\sqrt{2}} [f_D(m_+^2, m_-^2) \pm f_D(m_-^2, m_+^2)], \quad (9)$$

where $+$ ($-$) indicates a CP -even (CP -odd) state. Therefore, the expected number of events $\langle M_i^\pm \rangle$ in the i th bin of a sample that has been tagged with a decay that has a CP -even fraction F_+ is

$$\langle M_i^\pm \rangle = \epsilon_{DT,i} \frac{S_\pm}{2S_f} \left(K_i - 2c_i(2F_+ - 1)\sqrt{K_i K_{-i}} + K_{-i} \right), \quad (10)$$

where S_\pm (S_f) are the efficiency-corrected single-tag yields of the CP -eigenstate (flavor) modes used in the analysis and $\epsilon_{DT,i}$ is the DT efficiency in the i th bin. The value of F_+ is equal to 1 (0) for a pure CP -even (CP -odd) tag mode. We refer to modes with intermediate values of F_+ as quasi- CP tags. The values of c_i alone can be extracted using Eq. (10). The relation $s_i = \sqrt{1 - c_i^2}$ is a good approximation only for $N > 200$ [22], which is not feasible with the available data sample. However, analysing $D \rightarrow K_S^0 K^+ K^-$ decays tagged by $D \rightarrow K_S^0 h^+ h^-$ ($h = \pi, K$) decays gives access to both c_i and s_i . The amplitude of the $D^0 \bar{D}^0$ pair produced by the $\psi(3770)$ decaying to $K_S^0 K^+ K^-$ and $K_S^0 h^+ h^-$ is

$$f_D(m_+^2, m_-^2, \bar{m}_+^2, \bar{m}_-^2) = \frac{f_D(m_+^2, m_-^2) f_D(\bar{m}_-^2, \bar{m}_+^2) - f_D(\bar{m}_+^2, \bar{m}_-^2) f_D(m_-^2, m_+^2)}{\sqrt{2}}, \quad (11)$$

where $(\bar{m}_+^2, \bar{m}_-^2)$ are the Dalitz plot coordinates corresponding to the phase space of the $K_S^0 h^+ h^-$ decay. The expected event rate in which one D decays in the region of phase space defined by the i th bin of the $D \rightarrow K_S^0 K^+ K^-$ Dalitz plot and the other D in the region of phase space defined by the j th bin of the $D \rightarrow K_S^0 h^+ h^-$ Dalitz plot can be written as

$$\langle M_{ij} \rangle = \epsilon_{DT,ij} \frac{N_{D^0 \bar{D}^0}}{2S_f^2} \left(K_i K_{-j} + K_{-i} K_j - 2\sqrt{K_i K_{-j} K_{-i} K_j} (c_i c_j + s_i s_j) \right), \quad (12)$$

where $N_{D^0 \bar{D}^0}$ is the number of $D^0 \bar{D}^0$ pairs in the $\psi(3770)$ data sample and $\epsilon_{DT,ij}$ is the DT efficiency in the i th and j th

pair of bins. The two-fold ambiguity in the sign of s_i can be resolved using weak amplitude-model assumptions. Note that Eq. (10) is symmetric under the interchange of $i \leftrightarrow -i$ and Eq. (12) is symmetric under the interchange of pair, $(i, j) \leftrightarrow (-i, -j)$ and $(i, -j) \leftrightarrow (-i, j)$. No such symmetry exists for the values of K_i because $f_D(m_+^2, m_-^2) \neq f_D(m_-^2, m_+^2)$.

Ignoring the very low level of CP violation in the neutral kaon system, the K^0 state is an equal admixture of K_S^0 and K_L^0 states. Therefore, in the decays of correlated $D^0 \bar{D}^0$ pairs we expect a significant fraction of the D mesons to decay to the $K_L^0 K^+ K^-$ final state as well. Although so far γ has only been determined using $D \rightarrow K_S^0 h^+ h^-$ decays, the decay $D \rightarrow K_L^0 K^+ K^-$ has a close connection with $D \rightarrow$

$K_S^0 K^+ K^-$ that can be exploited to improve the precision with which c_i and s_i are determined. In the absence of CP violation, $CP|K_S^0\rangle = |K_S^0\rangle$ and $CP|K_L^0\rangle = -|K_L^0\rangle$. Hence $K_L^0 K^+ K^-$ has opposite CP to $K_S^0 K^+ K^-$. We define the decay amplitude for $D^0 \rightarrow K_L^0 K^+ K^-$ [$\bar{D}^0 \rightarrow K_L^0 K^+ K^-$] as $f'_D(m_+^2, m_-^2)$ [$f'_{\bar{D}}(m_+^2, m_-^2)$] such that

$$f'_D(m_+^2, m_-^2) = -f'_{\bar{D}}(m_-^2, m_+^2). \quad (13)$$

Therefore, the number of events in the i th bin of a CP - or quasi- CP tagged $D \rightarrow K_L^0 K^+ K^-$ sample is

$$\langle M_i^{\pm} \rangle = \epsilon'_{\text{DT},i} \frac{S_{\pm}}{2S'_f} \left(K'_i + 2c'_i(2F_+ - 1) \sqrt{K'_i K'_{-i} + K'_{-i}} \right), \quad (14)$$

where K'_i is defined in analogous fashion to K_i (see Eq. (4)). Furthermore, the expected event rate in the i th bin of the $D \rightarrow K_L^0 K^+ K^-$ Dalitz plot and the j th bin of the $D \rightarrow K_S^0 h^+ h^-$ Dalitz plot can be written as

$$\langle M'_{ij} \rangle = \epsilon'_{\text{DT},ij} \frac{N_{D\bar{D}}}{2S'_f S'_f} \left(K_i K'_{-j} + K_{-i} K'_j + 2\sqrt{K_i K'_{-j} K_{-i} K'_j} (c'_i c_j + s'_i s_j) \right). \quad (15)$$

The symmetries between the exchange of coordinates in the cases of M_i and M_{ij} are also present for M'_i and M'_{ij} . In general $(c_i, s_i) \neq (c'_i, s'_i)$ because $f'_D(m_+^2, m_-^2) \neq f_D(m_+^2, m_-^2)$. In order to improve the precision of the extracted values of c_i and s_i constraints are imposed on the difference $\Delta c_i = c'_i - c_i$ and $\Delta s_i = s'_i - s_i$; these constraints are explained in Sec. VIII.

III. BINNING OF THE $D^0 \rightarrow K_S^0 K^+ K^-$ DALITZ PLOT

All the relations given in Sec. II are independent of the shape of the Dalitz plot bins. The original proposal [8] was to divide the Dalitz plot into rectilinear bins. The reduction in sensitivity of such an approach compared to an unbinned analysis is about 30% even with 20 bins [22]. The sensitivity of the model-independent method as a function of the bin shape is discussed in Ref. [22]; this paper concludes that binning schemes that minimise the variations of $\Delta\delta_D$ within each Dalitz plot bin give significantly improved statistical sensitivity compared to the rectilinear binning. An amplitude model can be used to guide the definition of bin boundaries in order to minimize the $\Delta\delta_D$ variation. The number of bins that can be used in the analysis is restricted by the available statistics in either the $\psi(3770)$ or B -decay data samples. Since the use of an amplitude model is only to define the bin shapes, the model neither leads to any bias nor introduces any model-dependent uncertainties on the measurement of γ . However, a model that poorly describes the phase variation of the amplitude over the Dalitz plot may lead to a lower than expected statistical sensitivity to γ .

In the current analysis we employ an amplitude model for $D^0 \rightarrow K_S^0 K^+ K^-$ decays developed by the BaBar Collaboration [16] to define the bin shapes. Our choice of model and bin

definitions is consistent with the previous measurement [14]. The amplitude model is constructed in the isobar formalism, where the amplitude at a phase-space point is defined as a coherent sum of two-body amplitudes and a non-resonant amplitude. There are eight intermediate resonances used in the model. The $a_0(980)^0$ and $a_0(980)^\mp$ resonances are modelled by the Flatté parameterization [23], while all other resonances are parameterized by Breit-Wigner line shapes. The model-based lookup table (LUT) containing the moduli and phases of the $D^0 \rightarrow K_S^0 K^+ K^-$ amplitudes at different phase points ($m_-^2, M_{K^+ K^-}^2$) was supplied by the authors of Ref. [16]. The granularity of the ($m_-^2, M_{K^+ K^-}^2$) grid in the LUT is $0.00179 \text{ GeV}^2/c^4 \times 0.00536 \text{ GeV}^2/c^4$. Based on the LUT, the values of $\Delta\delta_D$ at a position (m_+^2, m_-^2) in the phase-space are calculated. Half of the Dalitz plot, $m_+^2 < m_-^2$, is divided into equally-spaced regions (bins) of $\Delta\delta_D$ satisfying the condition

$$2\pi(i - 3/2)/\mathcal{N} \leq \Delta\delta_D(m_+, m_-) < 2\pi(i - 1/2)/\mathcal{N}, \quad (16)$$

as shown in Fig. 1 for $\mathcal{N} = 2, 3$ and 4. Here $i = 1, 2, \dots, \mathcal{N}$ are the bin numbers. The bins in the region $m_+^2 > m_-^2$ are defined symmetrically. The class of binning defined by Eq. (16) is referred to as the “equal- $\Delta\delta_D$ ” binning scheme. A smaller number of bins is the best choice to measure c_i and s_i precisely, but this will potentially reduce the sensitivity to γ . On the other hand, a larger number of bins provides increased sensitivity to γ , because it is a better approximation to the unbinned method. Keeping this trade-off in mind, we perform the analysis with $\mathcal{N} = 2, 3$ and 4 bins. Binning the Dalitz plot with $\mathcal{N} > 4$ is not yet feasible with the size of the sample of $\psi(3770)$ data collected by BESIII; the fit to determine c_i and s_i described in Sec. VIII fails with $\mathcal{N} > 4$.

In order to ascertain the quality of the binning, a figure-of-merit based on the ratio of statistical sensitivity of the binned to the unbinned approach, known as the binning quality factor, \mathcal{Q} , is defined in Ref. [22]. The predicted values of \mathcal{Q} for this model are determined to be 0.771, 0.803 and 0.822 for $\mathcal{N} = 2, 3$ and 4 bins, respectively [14]. The measured values were $0.94^{+0.16}_{-0.06}$, $0.87^{+0.14}_{-0.06}$ and $0.94^{+0.21}_{-0.06}$ for $\mathcal{N} = 2, 3$ and 4 bins respectively [24]. Since these values are close to one it implies that the loss of sensitivity due to the current bin definitions is small. An optimal binning scheme, which accounts for the distribution of the B -meson data sample across the Dalitz plot, as well as the $\Delta\delta_D$ variation, is found to give negligible improvement to the projected sensitivity compared to the “equal- $\Delta\delta_D$ ” binning [14]; hence, it is not pursued further.

IV. BESIII DETECTOR AND EVENT GENERATION

We analyse an e^+e^- collision data sample produced by the Beijing Electron Positron Collider II (BEPCII), which corresponds to an integrated luminosity of 2.93 fb^{-1} [25], collected by the BESIII detector at a center-of-mass energy of $\sqrt{s} = 3.773 \text{ GeV}$. The BESIII experiment is a general purpose solenoidal detector with a geometrical acceptance of 93% of the 4π solid angle. It has a He-gas-based multilayer drift chamber (MDC) for measuring the momentum and specific

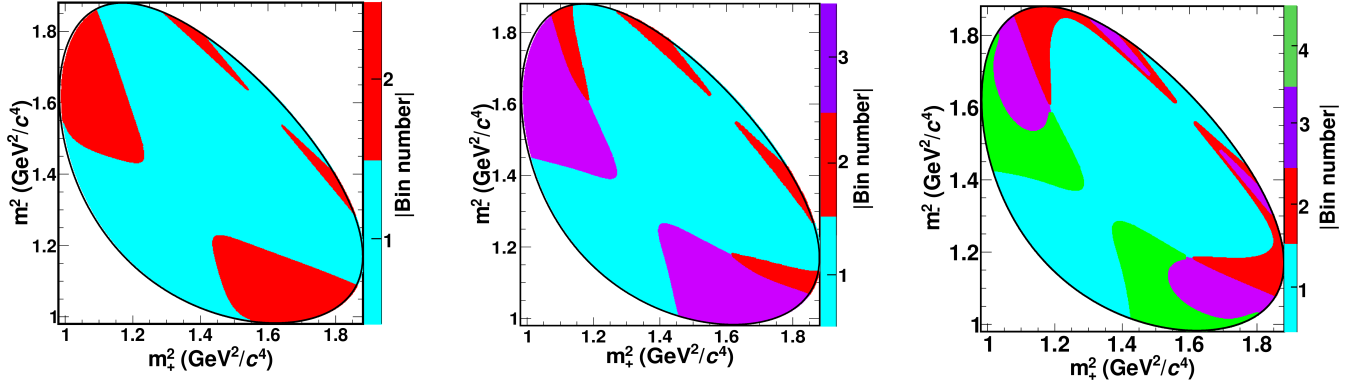


FIG. 1. Equal- $\Delta\delta_D$ binning of $D^0 \rightarrow K_S^0 K^+ K^-$ phase-space based on the BaBar model [16] for $\mathcal{N} = 2$ (left), $\mathcal{N} = 3$ (middle) and $\mathcal{N} = 4$ (right) bins. The color scale represents the absolute value of the bin number and the black curve represents the kinematic boundary of the Dalitz plot.

ionization loss (dE/dx) of the charged particles, a plastic-scintillator-based time-of-flight (TOF) measurement system for the identification of charged particles, and an electromagnetic calorimeter (EMC) consisting of CsI(Tl) crystal, which is used to measure the energy of the neutral showers and identify electrons. The detector is encapsulated in a magnetic field of 1 T provided by a superconducting solenoid. A resistive-plate-chamber-based muon counter is interleaved between the flux-return yoke of the magnet. The MDC has a transverse-momentum resolution of 0.5% at 1 GeV/c. The time resolution of the TOF is about 80 ps in the barrel region and 110 ps in the endcap region, enabling a 2σ K/π separation up to a momentum of 1 GeV/c. The energy resolution of the EMC for 1 GeV photons is about 2.5% in the barrel region and 5% in the endcap regions. More details about the BESIII detector can be found in Ref. [26].

Simulated samples produced with the GEANT4-based [27] Monte Carlo (MC) package, which includes the geometric description of the BESIII detector and the detector response, are used to determine the detection efficiency and to estimate the backgrounds. The simulation includes the beam-energy spread and initial-state radiation (ISR) in the e^+e^- annihilations modelled with the generator KKMC [28]. The inclusive MC samples consist of the production of $D\bar{D}$ pairs, the non- $D\bar{D}$ decays of the $\psi(3770)$, the ISR production of the J/ψ and $\psi(3686)$ states, and the continuum processes incorporated in KKMC [28]. The known decay modes are modelled with EVTGEN [29] using branching fractions taken from the Particle Data Group [30], and the remaining unknown decays from the charmonium states with LUNDCHARM [31]. The final state radiation (FSR) from charged final-state particles is incorporated with the PHOTOS package [32]. The simulation of quantum-correlations in the process $\psi(3770) \rightarrow D^0\bar{D}^0$ is done outside the EVTGEN framework, using an algorithm developed by the CLEO Collaboration [33]. The effective integrated luminosity of the generated $D^0\bar{D}^0$ sample is about ten times that of the data. For the efficiency determination we use signal MC samples. Signal MC samples consist of $D^0 \rightarrow S_{\text{tag}}, \bar{D}^0 \rightarrow X$ decays for the reconstruction of STs and $D^0 \rightarrow K_{S,L}^0 K^+ K^-, \bar{D}^0 \rightarrow S_{\text{tag}}$ decays for the recon-

struction of DTs, where S_{tag} is a tag final state and X is any inclusive final state. Each signal MC sample corresponds to a specific ST or DT decay mode studied in this paper and contains 2×10^5 events.

V. EVENT SELECTION

In this section we initially describe the requirements for selecting the reconstructed particles that are combined to form the final states of interest. Then we present the selection criteria of fully reconstructed tag modes and partially reconstructed tag modes in Secs. VA and VB, respectively.

Table I summarizes the set of tag modes used to reconstruct D^0 final states. The decay channels are split into five categories: Signal, Flavored, Mixed CP , CP -odd and CP -even. A highlight of this analysis is that the quasi- CP mode $D \rightarrow \pi^+\pi^-\pi^0$, which has a large branching fraction, is used for the first time for the strong-phase measurements in the $D \rightarrow K_{S,L}^0 K^+ K^-$ analysis. The F_+ value of $\pi^+\pi^-\pi^0$ is measured in Ref. [34] and the mode is found to be overwhelmingly CP -even. Hence in this analysis we treat $\pi^+\pi^-\pi^0$ as a CP -even tag taking into account its F_+ value. In the analysis, daughter particles are reconstructed as: $K_S^0 \rightarrow \pi^+\pi^-$, $\eta \rightarrow \gamma\gamma$, $\pi^0 \rightarrow \gamma\gamma$, $\omega \rightarrow \pi^+\pi^-\pi^0$, $\eta' \rightarrow \pi^+\pi^-\eta$. In this section we will describe the selection criteria implemented to reconstruct these final states.

TABLE I. D^0 decays used in this analysis.

Type	Tag modes
Signal	$K_S^0 K^+ K^-, K_L^0 K^+ K^-$
Flavored	$K^- \pi^+, K^- \pi^+ \pi^0, K^- e^+ \nu_e$
Mixed CP	$K_S^0 \pi^+ \pi^-, K_L^0 \pi^+ \pi^-$
CP -odd	$K_S^0 \pi^0, K_S^0 \eta, K_S^0 \eta', K_S^0 \omega$
CP -even	$K^+ K^-, \pi^+ \pi^-, \pi^+ \pi^- \pi^0, K_S^0 \pi^0 \pi^0,$ $K_L^0 \pi^0, K_L^0 \eta, K_L^0 \eta', K_L^0 \omega$

For the charged tracks the polar angle θ is required to be within the MDC acceptance, which is $|\cos \theta| < 0.93$. The

distance of closest approach of a primary track from the interaction region is required to be less than 10 cm in beam direction and less than 1 cm in the plane perpendicular to the beam direction to remove tracks not originating from e^+e^- collisions. For neutral showers the energy deposited in the EMC is required to be larger than 0.025 GeV in the barrel region ($|\cos\theta| < 0.8$) and larger than 0.050 GeV in the endcap region ($0.86 < |\cos\theta| < 0.92$), which reduces the effect of electronic noise and deposits resulting from beam-related backgrounds. Moreover, the angle between the position of the shower and any extrapolated charged track in the EMC must be greater than 10° to reduce the number of showers related to charged tracks. Furthermore, we require the time of the shower to be less than 700 ns after the event start-time to further suppress fake photons associated with electronic noise and beam backgrounds.

The particle identification (PID) is performed by combining the dE/dx information from the MDC as well as the time-of-flight of the charged particle. The likelihoods for the kaon hypothesis \mathcal{L}_K and pion hypothesis \mathcal{L}_π are calculated. Tracks satisfying the condition $\mathcal{L}_K > \mathcal{L}_\pi$ are identified as kaons and vice versa for pions. For electrons the PID is performed by defining a likelihood based on information about dE/dx in the MDC, time-of-flight and deposited energy and shape of the electromagnetic shower from the EMC. The track is identified as an electron if $\mathcal{L}_e/(\mathcal{L}_e + \mathcal{L}_K + \mathcal{L}_\pi) > 0.8$ and $\mathcal{L}_e > 0.001$, where \mathcal{L}_e is the likelihood of the electron hypothesis.

A K_S^0 candidate is formed by considering a pair of intersecting oppositely charged tracks. These tracks are not subject to any track quality requirement or PID. The closest approach of these tracks to the interaction point is required to be less than 20 cm along the beam direction with no requirement in the transverse direction. A secondary vertex fit is performed to form the K_S^0 vertex, and candidates with $\chi^2 < 100$ are selected. The updated four momenta after the secondary vertex fit are used later in this analysis. The mass of a K_S^0 candidate is required to be within the range (0.487, 0.511) GeV/c^2 . In order to suppress combinatorial backgrounds from two pions that are not from a true K_S^0 , the flight significance, L/σ_L , is required to be greater than two, where L is the flight length and σ_L is the uncertainty in L from the secondary vertex fit.

Both π^0 and η candidates are reconstructed from a pair of photons, where at least one of the photons must be reconstructed in the barrel region; this requirement reduces combinatorial backgrounds that arise from the large number of showers in the endcap region that are related to beam backgrounds. The invariant mass of the two photon candidates must be in the range (0.110, 0.155) GeV/c^2 or (0.480, 0.580) GeV/c^2 for π^0 and η candidates, respectively. In order to improve the momentum resolution, a kinematic fit of the two photons is performed with their invariant mass constrained to the nominal mass of π^0 or η meson taken from the PDG [30]. Only π^0 and η candidates with $\chi^2 < 20$ are selected. The improved values of the momenta are used later in the analysis. For ω candidates the invariant mass of the $\pi^+\pi^-\pi^0$ combination is required to be within the range (0.760, 0.805) GeV/c^2 and for η' candidates the invariant mass of the $\pi^+\pi^-\eta$ combination is required to be within the

range (0.938, 0.978) GeV/c^2 . All the invariant mass intervals described correspond to approximately ± 3 times the standard deviation about the mean of the reconstructed distribution.

A. Selection of fully reconstructed tags

Fully reconstructed tags are decay modes that do not contain an undetected particle in the final state. Before describing the kinematic variables used to select fully reconstructed tags, we introduce two additional vetoes that remove specific backgrounds to certain tag modes. The first veto is to suppress backgrounds arising from cosmic rays and lepton-pair events in the ST reconstruction of the two-body decay channels K^+K^- , $\pi^+\pi^-$ and $K^\pm\pi^\mp$. Here, we reject events in which the two charged tracks that reconstruct the ST candidate are consistent with being an e^+e^- or $\mu^+\mu^-$ pair. In addition, to suppress cosmic muons, we reject events where the time-of-flight difference between the two tracks is greater than 5 ns. Further, an event that has neither an EMC shower with an energy greater than 50 MeV nor an additional charged track in the MDC is rejected. The second veto is to remove the CP -odd $K_S^0\pi^0$, $K_S^0 \rightarrow \pi^+\pi^-$ background to the predominantly CP -even $\pi^+\pi^-\pi^0$ tag mode; here we reject events that satisfy the condition $|M_{\pi^+\pi^-} - m_{K_S^0}| < 0.018 \text{ GeV}/c^2$, where $m_{K_S^0}$ refers to the nominal mass of the K_S^0 meson given in Ref. [30].

For all fully reconstructed tag modes, the selected final-state particles are combined to reconstruct the D decay. Since the $D\bar{D}$ pair production occurs at the $\psi(3770)$ resonance, there are no additional particles in the final state, so the energy of each D meson is equal to $\sqrt{s}/2$. Thus, with a well measured beam energy $E_{\text{beam}} (= \sqrt{s}/2)$ we define two quantities to reconstruct the D candidates: the energy difference,

$$\Delta E \equiv \sum_i E_i - E_{\text{beam}}, \quad (17)$$

and the beam-constrained mass,

$$M_{\text{BC}} \equiv \frac{1}{c^2} \sqrt{E_{\text{beam}}^2 - \left| \sum_i \mathbf{p}_i c \right|^2}. \quad (18)$$

Here E_i and \mathbf{p}_i are the energies and momenta of the D decay products in the center-of-mass frame. Properly reconstructed candidates will peak at zero in the ΔE distribution and at the nominal mass of the D^0 meson [30] in the M_{BC} distribution. For all the reconstructed final states mode-dependent criteria are applied to the ΔE distribution to reduce the level of combinatorial backgrounds. The ΔE distribution is fit with a combination of a double-Gaussian function and a polynomial to describe the signal and background, respectively. The value of ΔE is required to be within the range $\pm 3\sigma$ [$(-4\sigma, 3\sigma)$] from the mean of the signal distribution for modes without [with] a π^0 in the final state. Here σ is the total width of the ΔE signal shape. If multiple ST candidates are reconstructed in an event, the candidate with the minimum value of $|\Delta E|$

is selected. If multiple DT candidates are selected, the candidate with a value $\bar{M} \equiv [M(D^0) + M(\bar{D}^0)]/2$ closest to the nominal D mass is selected.

B. Selection of partially reconstructed tags

Partially reconstructed tags collectively refer to the tag modes where there is one particle in the final state, either a K_L^0 meson or a neutrino, which is not reconstructed. Modes with more than one missing particle in the final state are not considered in this analysis. Due to the presence of a missing particle in the final state, these tag modes can be reconstructed only as DTs so that four-momentum conservation can be exploited in the reconstruction.

Selections of partially reconstructed tag modes proceed as follows. The opposite-side D candidate is reconstructed as a ST candidate using the criteria given in the Sec. V A. All the particles except the missing particle in the final state are reconstructed from the unused tracks and showers that satisfy the selection criteria already described. The presence of an unreconstructed K_L^0 is inferred from the missing-mass distribution, calculated from the missing energy, E_{miss} , and the missing momentum, \mathbf{p}_{miss} , in the center-of-mass frame as

$$M_{\text{miss}}^2 \equiv \frac{E_{\text{miss}}^2}{c^4} - \frac{|\mathbf{p}_{\text{miss}}|^2}{c^2}, \quad (19)$$

which peaks at $m_{K^0}^2$ for signal, where m_{K^0} is the nominal mass of the neutral kaon given in Ref. [30]. The presence of a neutrino is inferred using the variable

$$U_{\text{miss}} \equiv E_{\text{miss}} - |\mathbf{p}_{\text{miss}}|c, \quad (20)$$

which peaks at zero for signal. Again we take advantage of resonant production and the knowledge of beam energy to determine E_{miss} and \mathbf{p}_{miss} . Figure 2 shows example distributions of M_{miss}^2 and U_{miss} . Reconstruction using the missing-mass technique inevitably results in a higher level of background than the full-reconstruction method. To reduce the background further, we do not consider events that have more charged tracks or neutral particles than required in the final state. The angle, α , between the \mathbf{p}_{miss} and the nearest unassigned shower is calculated. All the events with $\cos \alpha > 0.98$ are retained. For the events with $\cos \alpha < 0.98$ mode-dependent criteria are applied on the energy of the unassigned shower. Even though we reject events with additional neutral particles in the final state, there is significant background in the modes with neutral particles in the final states, arising from the final states having additional neutral particles that are not reconstructed. For example, in the case of $D \rightarrow K_L^0 \pi^0$ decays there are backgrounds from $K_L^0 \pi^0 \pi^0$ where one π^0 meson is not reconstructed, so the event passes all our selection criteria. These backgrounds can be further reduced by applying criteria on the momentum spectrum of reconstructed π^0 or η candidates wherever applicable. The values of these criteria are selected based on optimization studies that use the inclusive MC samples. This optimization maximizes the figure-of-merit defined as $S/\sqrt{S+B}$, where S (B) are the number of

signal (background) events in the signal region retained by the selection; the signal region for the optimization is the interval $0.2 < M_{\text{miss}}^2 < 0.3 \text{ GeV}^2/c^4$. The values of the shower energy and π^0 (η) momentum criteria are varied, and the value that maximizes the figure-of-merit is chosen.

VI. ESTIMATION OF ST AND DT YIELDS

In Secs. VI A and VI B we will describe the methods of estimating ST and DT yields, respectively. Note that DT yields are only required bin-by-bin, not integrated over the Dalitz plot.

A. ST yields

ST yields of fully reconstructed tag modes are determined from maximum likelihood fits to the M_{BC} distribution. Our probability density function (PDF) is a sum of the signal shape derived from the signal MC sample convolved with a Gaussian function to account for any difference in resolution between data and MC simulation, and an ARGUS function [35] to model the background. The threshold of the ARGUS function is fixed at $M_{BC} = 1.8865 \text{ GeV}/c^2$, which corresponds to the kinematic limit of D^0 production at the $\psi(3770)$. The peaking background is modelled by the shapes and yields obtained from the inclusive MC sample; this assumption is considered as a source of systematic uncertainty. The flavor-tag modes $D^0 \rightarrow K^-\pi^+$ and $D^0 \rightarrow K^-\pi^+\pi^0$ have a peaking background of approximately 0.2% from DCS decays. The dominant peaking background to the decays $D \rightarrow K_S^0 \pi^0$ and $D \rightarrow K_S^0 \pi^0 \pi^0$ is from $D \rightarrow \pi^+\pi^-\pi^0$ (0.5%) and $D \rightarrow \pi^+\pi^-\pi^0\pi^0$ (7%) decays, respectively. The M_{BC} distribution is fit over the range (1.83, 1.88) GeV/c^2 . The ST yields are obtained by integrating the M_{BC} distribution in the range (1.86, 1.87) GeV/c^2 . In order to eliminate the small effect of $D^0 \bar{D}^0$ mixing, the measured ST yields of CP modes are multiplied by a correction factor of $1/(1 - \eta_{\pm} y_D)$, where η_{\pm} is the CP eigenvalue of the mode and y_D is the charm-mixing parameter taken from Ref. [30].

The ST yield, S_{ST} , of a partially reconstructed tag is calculated using the relation

$$S_{\text{ST}} = 2N_{D^0 \bar{D}^0} \mathcal{B}_{\text{ST}}, \quad (21)$$

where $N_{D^0 \bar{D}^0}$ is the number of $D^0 \bar{D}^0$ pairs in the BESIII data sample [36] and \mathcal{B}_{ST} is the branching fraction of the tag mode, which is taken from Ref. [30] where available. The branching fractions of all $D \rightarrow K_L^0 X$ modes except $D \rightarrow K_L^0 \pi^0$ are not available in Ref. [30], hence we assume the branching fractions of these modes to be the same as for the corresponding $D \rightarrow K_S^0 X$ modes. We note that this reasoning is not strictly valid, as the interference between Cabibbo-favored (CF) ($D^0 \rightarrow \bar{K}^0 X$) and DCS transitions ($D^0 \rightarrow K^0 X$) can lead to a difference in the decay rates for $D \rightarrow K_L^0 X$ and $D \rightarrow K_S^0 X$. However, this difference is expected to be less than 10% [37], which is considered as a systematic uncertainty; the difference will barely affect our final results, as the

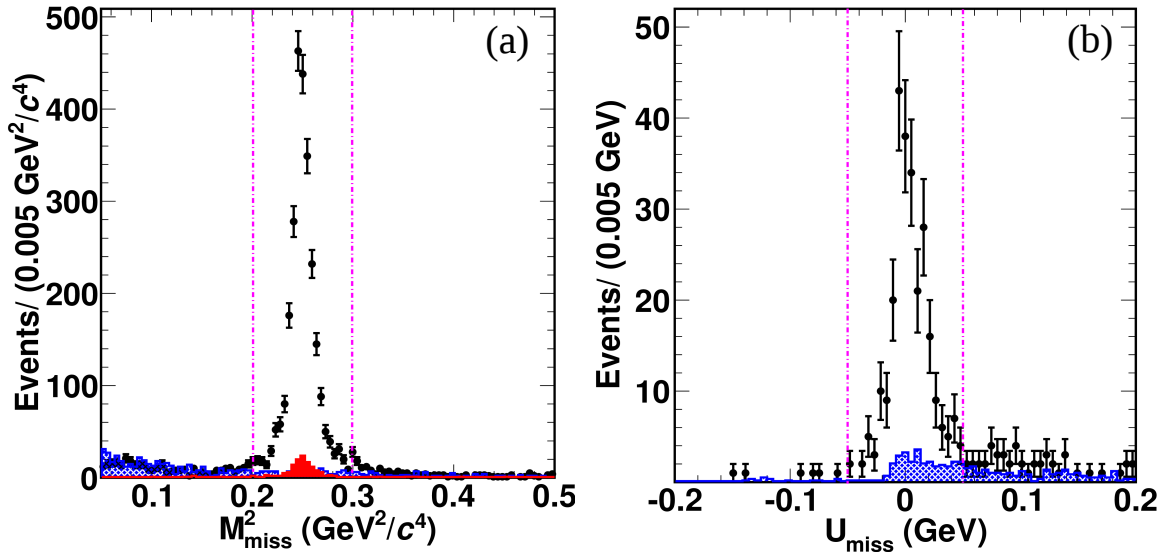


FIG. 2. (a) M_{miss}^2 distribution for $\bar{D}^0 \rightarrow K_L^0 K^+ K^-$ candidates reconstructed against the flavor-tags $D^0 \rightarrow K^- \pi^+$ and $D^0 \rightarrow K^- \pi^+ \pi^0$. The points with error bars are the data, the red histogram denotes the peaking background due to $\bar{D}^0 \rightarrow K_S^0 K^+ K^-$ events from the inclusive MC sample, the blue-shaded histogram shows the combinatorial backgrounds from inclusive MC samples, and the magenta vertical lines indicates the signal region. (b) U_{miss} distribution for events in which $\bar{D}^0 \rightarrow K_S^0 K^+ K^-$ candidates are reconstructed against the $D^0 \rightarrow K^- e^+ \nu_e$ tag. The black points with error bars are data, the blue-shaded histogram shows the backgrounds estimated from the inclusive MC sample and the magenta vertical line shows the signal region.

ST yields are used only for yield normalisation, as given in Eqs. (10) and (14). The ST yields calculated using Eq. (21) have larger uncertainties compared to the fully reconstructed tags, largely due to the uncertainty of the assumed values of \mathcal{B}_{ST} . The ST M_{BC} fits are shown in Fig. 3 and the yields are given in Table II. The effect on the final measurement due to the uncertainty in the measured values of the ST yields is treated as a systematic uncertainty. The ST yield uncertainty includes systematic uncertainties related to the fit procedure.

B. DT yield

For fully reconstructed DT modes we follow a sideband-estimation method developed by the CLEO Collaboration [38] to determine the DT yield. The sidebands are defined on the two-dimensional $(M_{\text{BC}}^{D^0}, M_{\text{BC}}^{\bar{D}^0})$ plane as shown in Fig. 4. Here, the $M_{\text{BC}}^{D^0}$ ($M_{\text{BC}}^{\bar{D}^0}$) refers to the M_{BC} distribution of signal (tag) side. In Fig. 4, S refers to the signal region, sideband A (B) contains events which are from misreconstructed tag (signal) decays, sideband C consists of continuum events and sideband D consists of events that are purely combinatoric. The amount of combinatorial (non-peaking) backgrounds in the signal region is estimated from the events in the sideband regions. Thus the total DT yield, N_{DT} , of $K_S^0 K^+ K^-$ is estimated as

$$N_{\text{DT}} = N_S - N_P - \left(\frac{a_S}{a_D} N_D + \sum_{i=A,B,C} \frac{a_S}{a_i} \left(N_i - \frac{a_S}{a_i} N_D \right) \right), \quad (22)$$

where a_i is the area of the corresponding region $i = A, B, C, D$ or S, N_i refers to the yields in the sideband region, N_S is the yield in the signal region before background correction (uncorrected yield) and N_P is the peaking-background yield estimated from the MC simulation (see Sec. VII B).

In the case of partially reconstructed tag modes we follow a similar sideband-estimation method as in Ref. [24]. Here three regions are defined on the M_{miss}^2 or U_{miss} distributions: low sideband (L), signal region (S) and high sideband (H). The total yield is estimated as

$$Y_S = \frac{(N_S - N_S^P) - \delta(N_L - N_L^P) - \gamma(N_H - N_H^P)}{1 - \delta\alpha - \gamma\beta}, \quad (23)$$

where N_S , N_L and N_H are the uncorrected yields in the signal and sideband regions, N_i^P refers to the peaking background in the i th region, δ and γ refer to the ratio of combinatorial backgrounds in the signal region to that in the L and H sideband regions, respectively, and α and β refer to the ratio of signal in region S to that in the regions L and H, respectively. The values of α , β , δ and γ are derived from MC samples. Here the definitions of sidebands are mode dependent. We follow the same optimization procedure described in Sec. VB to define the signal regions. The peaking backgrounds are estimated from MC samples as described in Sec. VII B.

VII. $D \rightarrow K_{S,L}^0 K^+ K^-$ DALITZ PLOTS

In this section we discuss the Dalitz plot distributions of events when $D \rightarrow K_{S,L}^0 K^+ K^-$ candidates are tagged with

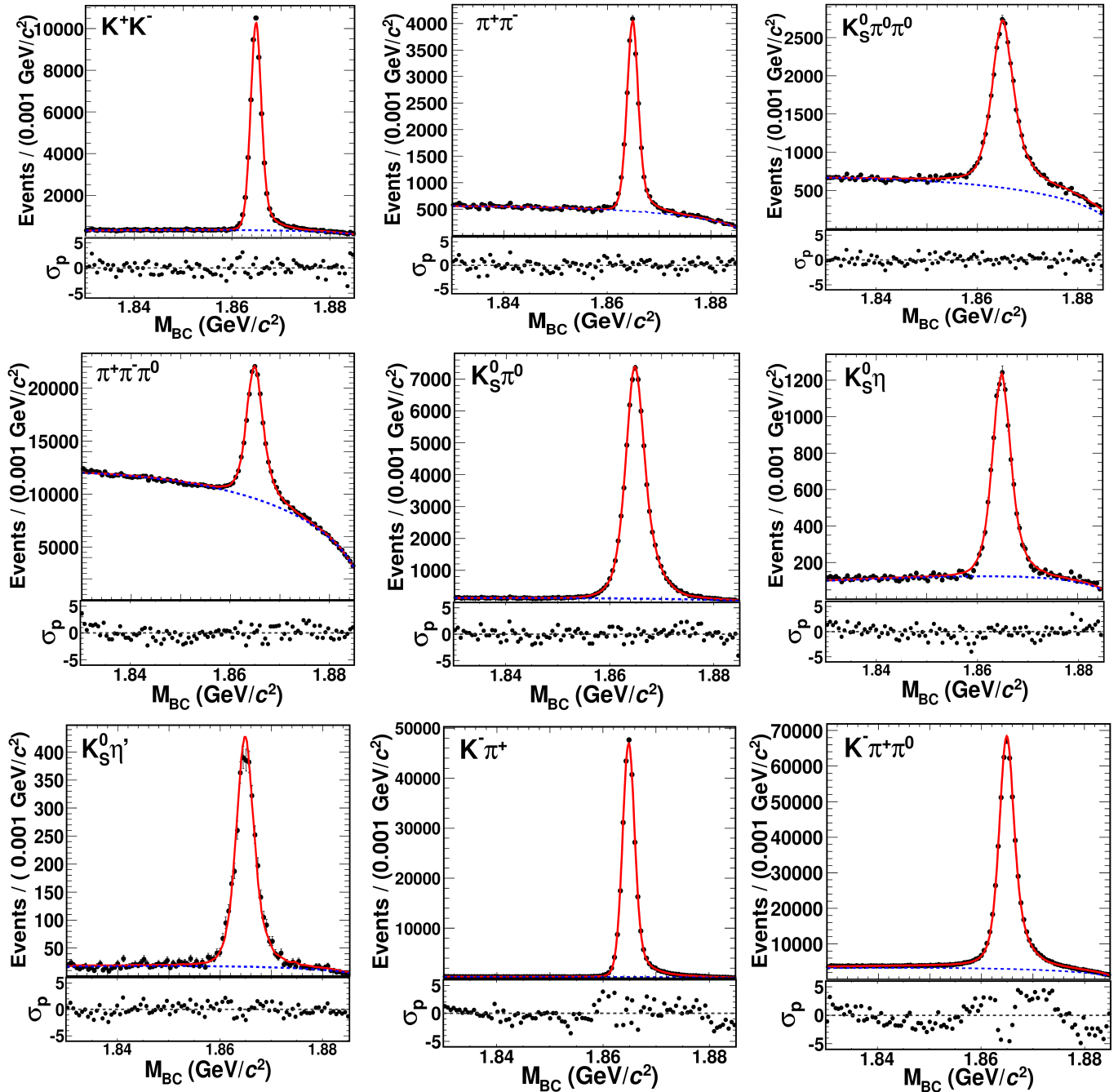


FIG. 3. Fits to the M_{BC} distributions of ST decay modes. The points with error bars are data, the red curve is the total fit result and the blue dashed curve is the background component. Beneath each distribution the pull (σ_p) between the data and the fit is shown. The significant pulls observed in the flavor-tag modes $D^0 \rightarrow K^- \pi^+$ and $D^0 \rightarrow K^- \pi^+ \pi^0$ are a consequence of the large sample size but studies of MC samples indicate that there is no significant bias on the ST yield introduced as a result.

pure CP eigenstates and mixed CP states; we highlight the important differences.

In order to improve the resolution on the Dalitz plot variables (m_+^2, m_-^2), a kinematic fit is performed for $D \rightarrow K_{S,L}^0 h^+ h^-$ candidates. For $D \rightarrow K_S^0 h^+ h^-$ tags, the two pions from the K_S^0 candidate obtained after the secondary vertex fit are combined with the h^+ and h^- into a common fit to the

nominal mass of the D^0 meson taken from Ref. [30]. In the case of a $D \rightarrow K_L^0 h^+ h^-$ candidate, a missing particle is created using the position of an EMC shower associated with the K_L^0 candidate. The mass of this object is set to the nominal mass of the K_L^0 meson taken from Ref. [30]; it is combined with $h^+ h^-$ tracks and fit to the nominal mass of the D^0 meson. A 35 to 40% (30 to 35%) improvement in the m_{\pm}^2 reso-

TABLE II. Single-tag (ST) and $D^0 \rightarrow K_{S,L}^0 K^+ K^-$ double-tag (DT) yields and efficiencies. The DT yields are the observed number of events in the signal region prior to background and efficiency corrections. The ST yields are background subtracted because they are the result of fits to the M_{BC} distributions.

Mode	ST		DT			
	N_{ST}	$\epsilon_{ST}(\%)$	$N_{DT}^{K_S^0 K^+ K^-}$	$N_{DT}^{K_L^0 K^+ K^-}$	$\epsilon_{DT}^{K_S^0 K^+ K^-}(\%)$	$\epsilon_{DT}^{K_L^0 K^+ K^-}(\%)$
Flavor-tags						
$K^- \pi^+$	524307 ± 742	63.31 ± 0.06	323	743	12.43 ± 0.07	15.85 ± 0.08
$K^- \pi^+ \pi^0$	995683 ± 1117	31.70 ± 0.03	596	1769	5.86 ± 0.05	7.94 ± 0.06
$K^- e^+ \nu_e$	752387 ± 12795		263		3.23 ± 0.04	
CP-even tags						
$K^+ K^-$	53481 ± 247	61.02 ± 0.11	42	112	12.07 ± 0.07	15.52 ± 0.08
$\pi^+ \pi^-$	19339 ± 163	64.52 ± 0.11	10	31	12.16 ± 0.07	15.70 ± 0.08
$K_S^0 \pi^0 \pi^0$	19882 ± 233	14.86 ± 0.08	7	45	2.49 ± 0.04	3.79 ± 0.04
$\pi^+ \pi^- \pi^0$	99981 ± 618	37.65 ± 0.11	51	254	6.79 ± 0.06	9.54 ± 0.07
$K_L^0 \pi^0$	209445 ± 14796		90		8.88 ± 0.06	
$K_L^0 \eta(\gamma\gamma)$	40009 ± 2543		19		6.60 ± 0.06	
$K_L^0 \omega$	207376 ± 11498		44		3.42 ± 0.04	
$K_L^0 \eta'(\pi^+ \pi^- \eta)$	33683 ± 1909		7		3.23 ± 0.04	
CP-odd tags						
$K_S^0 \pi^0$	65072 ± 281	36.92 ± 0.11	39	89	6.75 ± 0.06	9.33 ± 0.07
$K_S^0 \eta(\gamma\gamma)$	9524 ± 134	32.94 ± 0.11	9	10	6.05 ± 0.05	9.05 ± 0.06
$K_S^0 \omega$	19262 ± 157	12.14 ± 0.07	16	27	2.20 ± 0.03	3.42 ± 0.04
$K_S^0 \eta'(\pi^+ \pi^- \eta)$	3301 ± 62	12.46 ± 0.07	2	5	2.20 ± 0.03	3.46 ± 0.04
Mixed CP tags						
$K_S^0 \pi^+ \pi^-$			78	265	6.35 ± 0.05	8.32 ± 0.06
$K_L^0 \pi^+ \pi^-$			282		9.56 ± 0.07	
$K_S^0 K^+ K^-$	12949 ± 119	18.35 ± 0.09	4	19	2.99 ± 0.04	3.40 ± 0.04

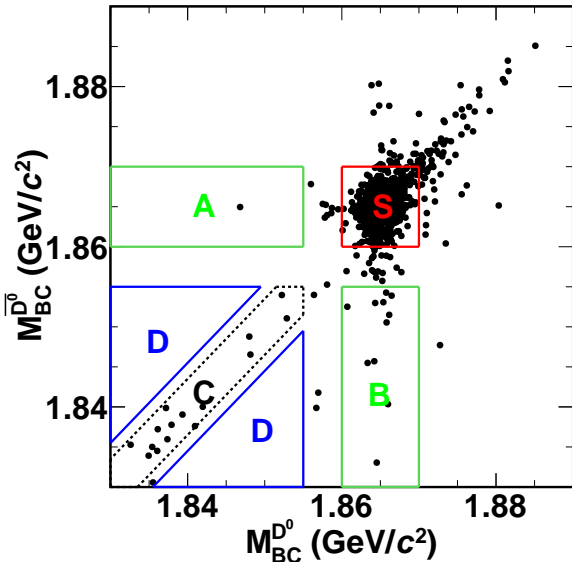


FIG. 4. Distribution of events across $(M_{BC}^{D^0}, M_{BC}^{\bar{D}^0})$ plane for $K_S^0 K^+ K^-$ reconstructed against flavor-tags. The signal region is denoted as S, while A, B, C and D are the various sideband regions.

lution across the Dalitz plot is achieved for $D \rightarrow K_S^0 K^+ K^-$ ($D \rightarrow K_L^0 K^+ K^-$) candidates after the kinematic fit. The resolutions are quantified using the signal MC samples. Events that fail the kinematic fit are rejected. The improved values of

(m_+^2, m_-^2) are used to define the position of the event within the Dalitz plot and assign its bin index.

The Dalitz plot distribution of the $D \rightarrow K_S^0 K^+ K^-$ candidates reconstructed against CP -even tag modes and their corresponding $M_{K^+ K^-}^2$ projections are given in Fig. 5. The presence of a significant peak around $M_{K^+ K^-}^2 \sim 1.04 \text{ GeV}^2/c^4$ is due to the decay $D^0 \rightarrow K_S^0 \phi$, $\phi \rightarrow K^+ K^-$. These events are distributed along the diagonal boundary of the Dalitz plot. As $D^0 \rightarrow K_S^0 \phi$ constitutes a large fraction of the total $D^0 \rightarrow K_S^0 K^+ K^-$ decay width [30], a higher population of events is seen in the region enclosing the ϕ resonance. A similar peak is absent in the $M_{K^+ K^-}^2$ distribution of $D \rightarrow K_S^0 K^+ K^-$ candidates reconstructed against CP -odd tag modes shown in Figs. 5(c) and (d). This is a consequence of the quantum-correlation in data. Since each D meson is of opposite CP eigenvalue, the $K_S^0 K^+ K^-$ candidates reconstructed against CP -odd tags should decay through CP -even intermediate states. Hence it cannot decay through the $D \rightarrow K_S^0 \phi$ state. The dominant CP -even intermediate state is the $D \rightarrow K_S^0 a(980)^0$ decay. The distribution of events in the Dalitz plot is observed to be flatter than in the case of $K_S^0 K^+ K^-$ tagged against a CP -even state. Since K_S^0 and K_L^0 have opposite CP eigenvalues, the entire scenario is reversed in the case of $D \rightarrow K_L^0 K^+ K^-$ decays as shown in Fig. 6. The Dalitz plot distribution of $D \rightarrow K_L^0 K^+ K^-$ candidates against CP -even modes resembles that of $D \rightarrow K_S^0 K^+ K^-$ candidates against CP -odd modes and vice versa.

The Dalitz plot distribution of $D \rightarrow K_L^0 K^+ K^-$ candidates

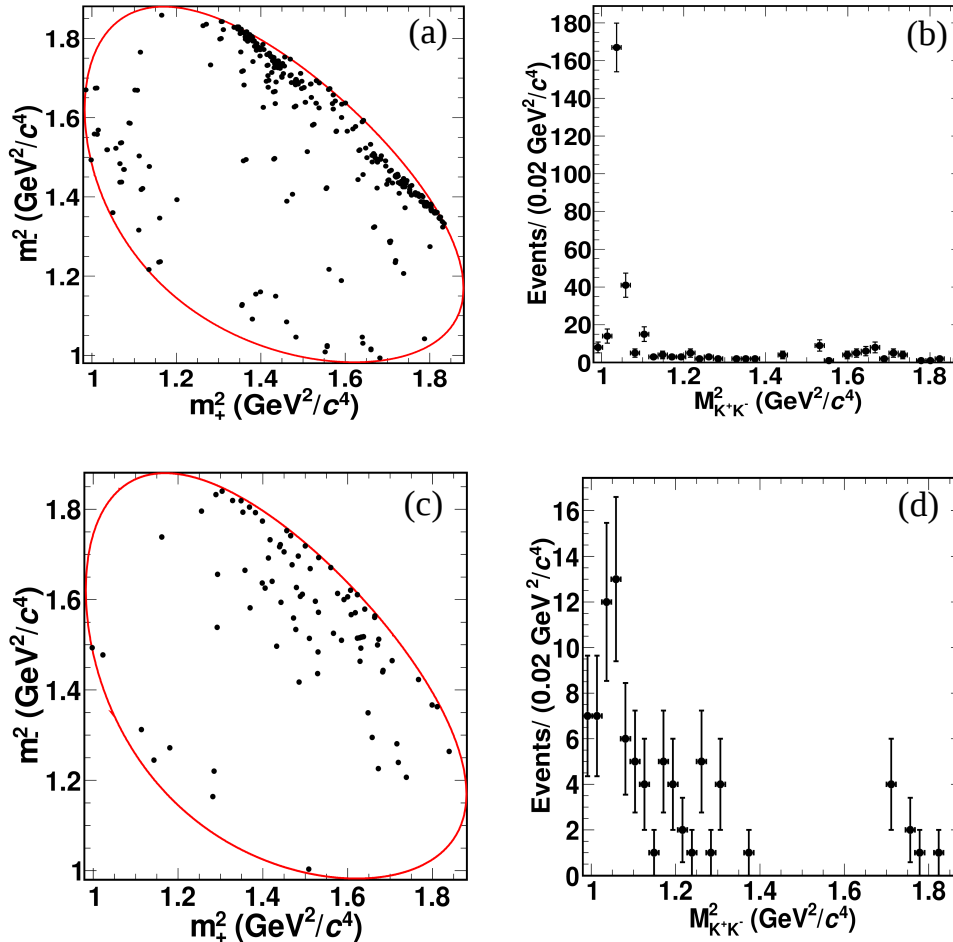


FIG. 5. (a) Dalitz plot and (b) $M_{K^+K^-}^2$ distributions for $D \rightarrow K_S^0 K^+ K^-$ reconstructed against CP -even final states. (c) Dalitz plot and (d) $M_{K^+K^-}^2$ distributions for $D \rightarrow K_S^0 K^+ K^-$ reconstructed against CP -odd final states.

against the self-conjugate mode $D \rightarrow K_S^0 \pi^+ \pi^-$ is given separately for signal and tag sides in Fig. 7. The Dalitz plot of $D \rightarrow K_S^0 \pi^+ \pi^-$ tags is consistent with that presented in Ref. [13]. In Fig. 7(d), the enhancement above $M_{\pi^+ \pi^-}^2 \sim 1.3$ GeV^2/c^4 corresponds to $D \rightarrow K^*(892)^\pm \pi^\mp$ decays, whereas the peak around $M_{\pi^+ \pi^-}^2 \sim 0.6$ GeV^2/c^4 corresponds to $D \rightarrow K_S^0 \rho^0$ decays. The $D \rightarrow K^*(892)^\pm \pi^\mp$ decays can be seen as two bands that are parallel to the vertical and horizontal axes of the Dalitz plane. The decay $D \rightarrow K_S^0 \rho^0$ lies close and parallel to the diagonal boundary. Since the $D \rightarrow K_L^0 K^+ K^-$ decays reconstructed against $D \rightarrow K_S^0 \pi^+ \pi^-$ decays are not in a CP eigenstate, the Dalitz plot distribution is a combination of both the CP -even and CP -odd tagged $K_L^0 K^+ K^-$ Dalitz plots. The Dalitz plot structure of $D \rightarrow K_S^0 K^+ K^-$ reconstructed against $D \rightarrow K_{S,L}^0 \pi^+ \pi^-$ has similar features to those shown in Fig. 7.

A. Dalitz plot binning, bin yield estimation and corrections

In this section we describe our method of binning the Dalitz plots and calculating the bin yields and efficiencies. The pro-

cedures for correcting the bin migration and DCS correction for flavor-tag yields are also explained.

The binning prescription followed in our analysis is described in Sec. II. The entire $D^0 \rightarrow K_{S,L}^0 K^+ K^-$ Dalitz plot is divided into $\mathcal{N} = 2$, $\mathcal{N} = 3$ and $\mathcal{N} = 4$ equal- $\Delta\delta_D$ bins. In the case of $D \rightarrow K_{S,L}^0 \pi^+ \pi^-$ tag modes, the entire Dalitz plot is divided into $\mathcal{N} = 8$ equal- $\Delta\delta_D$ bins identical to those defined in Ref. [13]. The uncorrected bin yields are obtained by counting the number of events in each bin. The bin yield M_i^\pm (see Eq. (10)) of $D \rightarrow K_S^0 K^+ K^-$ reconstructed against CP tags and the flavor-tag yield, K_i (see Eq. (4)) are calculated separately for each mode. The events in the i th bin of the $D \rightarrow K_S^0 K^+ K^-$ Dalitz plot and the j th bin of the $D \rightarrow K_S^0 h^+ h^-$ Dalitz plot are counted to obtain M_{ij} (see Eq. (12)). A similar procedure is followed to obtain the yields K'_i , $M_i^{\pm'}$ and M'_{ij} (see Eqs. (14) and (15)) for the $D \rightarrow K_L^0 K^+ K^-$ decay. The flavor-tag yield for the $D^0 \rightarrow K_{S,L}^0 \pi^+ \pi^-$ mode is taken from Ref. [13]. The yields of $D \rightarrow K_S^0 K^+ K^-$ decays reconstructed against CP tags are quite low. The inclusion of the $D \rightarrow \pi^+ \pi^- \pi^0$ tag mode results in an approximately 50% increase in the CP -even tag yield. The uncorrected yields of $D \rightarrow K_S^0 K^+ K^-$ decays re-

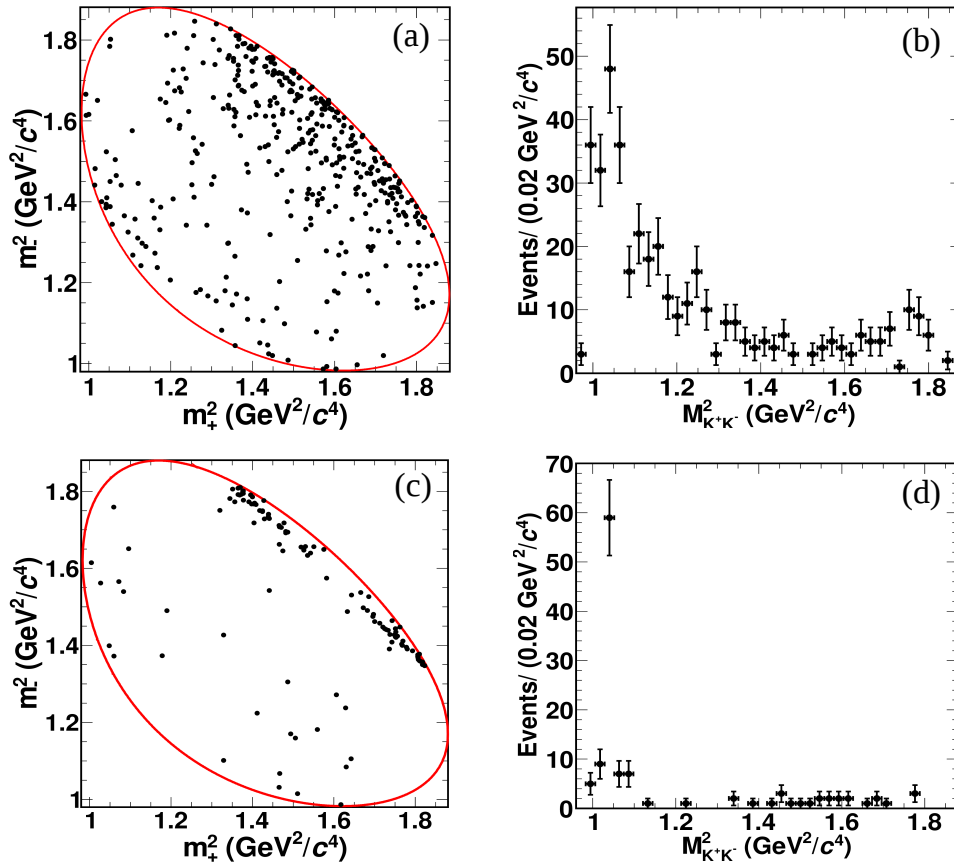


FIG. 6. (a) Dalitz plot and (b) $M_{K^+K^-}^2$ distributions for $D \rightarrow K_L^0 K^+ K^-$ reconstructed against CP -even final states. (c) Dalitz plot and (d) $M_{K^+K^-}^2$ distributions for $D \rightarrow K_L^0 K^+ K^-$ reconstructed against CP -odd final states.

constructed against CP tags, along with their efficiencies, are given in Table II.

Due to the finite (m_+^2, m_-^2) resolution, events migrate between bins. Often these migrations are asymmetric between the bins because of the differing event densities in each bin. We correct for this using an unfolding method based on correction factors derived from the signal MC samples. For $D \rightarrow K_{S,L}^0 K^+ K^-$ decays reconstructed against CP and flavor tags, we define a $2\mathcal{N} \times 2\mathcal{N}$ migration matrix \mathbf{U} as

$$U_{i,j} \equiv \frac{m_{ji}}{\sum_{k=-\mathcal{N}, k \neq 0}^{\mathcal{N}} m_{jk}}, \quad (24)$$

where m_{ji} are the events generated in the j th bin and reconstructed in the i th bin. The vector of migration-corrected data yields \mathbf{N} and the vector of reconstructed yields in the signal region \mathbf{N}_S are related by

$$\mathbf{N} = \mathbf{U}^{-1} \mathbf{N}_S. \quad (25)$$

In the case of $D \rightarrow K_{S,L}^0 K^+ K^-$ reconstructed against the $D \rightarrow K_{S,L}^0 h^+ h^-$ tags, the correlation between the bins on the signal and tag sides needs to be taken into account. Hence the total migration matrix is a tensor (Kronecker) product of signal- and tag-migration matrices. For a given number of signal bins \mathcal{N} , the dimension of the migration matrix for

$K_{S,L}^0 K^+ K^-$ against $K_{S,L}^0 K^+ K^-$ is $4\mathcal{N}^2 \times 4\mathcal{N}^2$ and for $K_{S,L}^0 K^+ K^-$ against $K_{S,L}^0 \pi^+ \pi^-$ it is $32\mathcal{N} \times 32\mathcal{N}$. The uncertainties in the matrix elements due to the finite size of the signal MC sample are considered as a source of systematic uncertainty. An example of the migration matrix for $D \rightarrow K_S^0 K^+ K^-$ candidates reconstructed against the $D \rightarrow K^+ K^-$ tag mode is given in Table III. Typically the rate of migration out of bin 1, which contains the narrow ϕ resonance, is about 3% for $D \rightarrow K_S^0 K^+ K^-$ decays and about 5% for $D \rightarrow K_L^0 K^+ K^-$ decays. The rate of migration into bin 1 is significantly smaller due to the broader structures that occupy the remainder of the Dalitz plot away from the ϕ resonance. Throughout this unfolding procedure we assume signal and background migrate in identical fashion, because the background is dominated by peaking components.

The bin efficiency for each tag mode is evaluated from the signal MC sample. The signal MC yield in each bin is corrected for migration before calculating the efficiency. The bin efficiency is defined as the ratio of events reconstructed in each bin to the number of events generated. The bins are combined appropriately taking into account their symmetry (see Sec. II) when estimating the efficiencies. The total DT efficiencies are given in Table II. In the case of $D \rightarrow K_S^0 K^+ K^-$, the efficiencies vary between $(12.43 \pm 0.07)\%$ for $K_S^0 K^+ K^-$ vs. $K^- \pi^+$ tags to $(2.20 \pm 0.03)\%$ for $K_S^0 K^+ K^-$ vs. $K_S^0 \eta'$ tags,

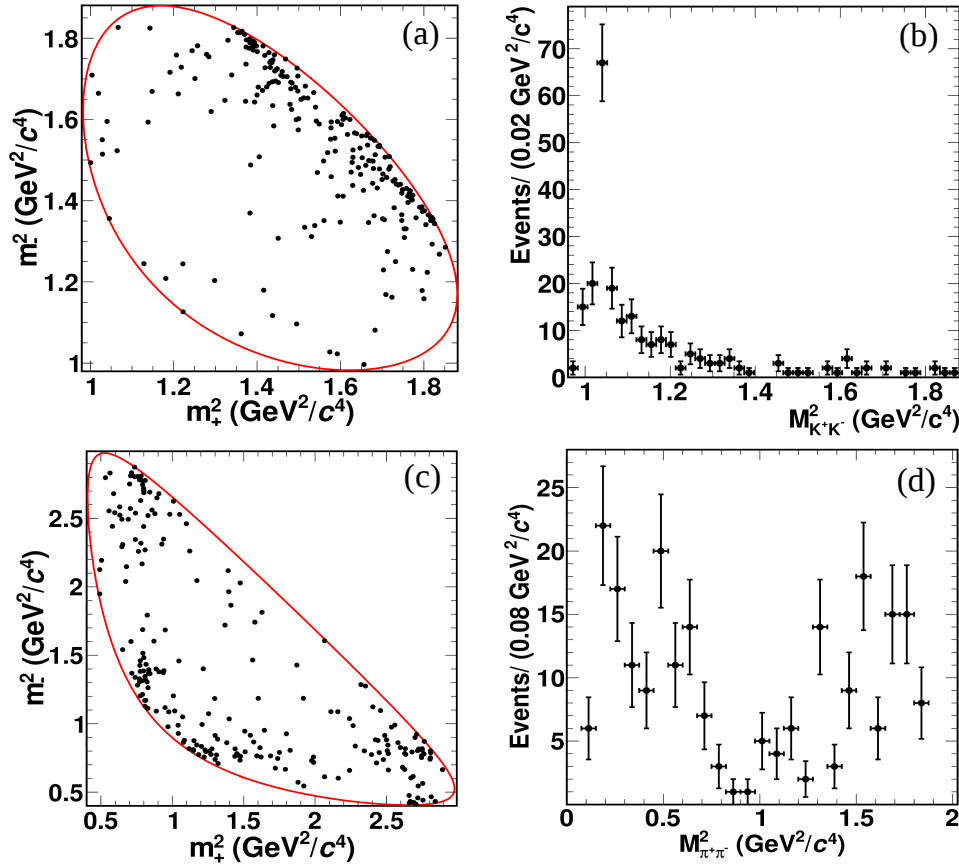


FIG. 7. (a) Dalitz plot and (b) $M_{K^+K^-}^2$ distributions for $D \rightarrow K_L^0 K^+ K^-$ reconstructed against $\bar{D} \rightarrow K_S^0 \pi^+ \pi^-$ final states. (c) Dalitz plot and (d) $M_{\pi^+\pi^-}^2$ distributions for $\bar{D} \rightarrow K_S^0 \pi^+ \pi^-$ decay in the same events.

TABLE III. Migration matrix for $K_S^0 K^+ K^-$ vs. $K^+ K^-$ events when the $D \rightarrow K_S^0 K^+ K^-$ Dalitz plot is divided into $\mathcal{N} = 3$ bins.

i	$U_{i,1}$	$U_{i,2}$	$U_{i,3}$	$U_{i,-1}$	$U_{i,-2}$	$U_{i,-3}$
1	0.968	0.020	0.001	0.011	0.000	0.000
2	0.036	0.967	0.001	0.000	0.001	0.003
3	0.007	0.001	0.992	0.000	0.000	0.000
-1	0.010	0.000	0.000	0.972	0.018	0.000
-2	0.000	0.000	0.000	0.032	0.967	0.001
-3	0.000	0.000	0.000	0.006	0.006	0.988

whereas for $D \rightarrow K_L^0 K^+ K^-$ the efficiency varies between

$$f_i^F = \frac{\int_i |f(m_+^2, m_-^2)|^2 dm_+^2 dm_-^2}{\int_i (|f(m_+^2, m_-^2)|^2 + (r_D^F)^2 |f(m_-^2, m_+^2)|^2 - 2r_D^F R_F \mathcal{R}[e^{i\delta_D^F} f(m_+^2, m_-^2) f^*(m_-^2, m_+^2)]) dm_+^2 dm_-^2}, \quad (26)$$

$$f_i^{F'} = \frac{\int_i |f'(m_+^2, m_-^2)|^2 dm_+^2 dm_-^2}{\int_i (|f'(m_+^2, m_-^2)|^2 + (r_D^F)^2 |f'(m_-^2, m_+^2)|^2 + 2r_D^F R_F \mathcal{R}[e^{i\delta_D^F} f'(m_+^2, m_-^2) f'^*(m_-^2, m_+^2)]) dm_+^2 dm_-^2}, \quad (27)$$

where r_D^F is the ratio of the moduli of the DCS to CF am-

(15.85 \pm 0.08)% for $K_L^0 K^+ K^-$ vs. $K^- \pi^+$ tags and (3.40 \pm 0.04)% for $K_S^0 K^+ K^-$ vs. $K_L^0 K^+ K^-$ tags. The uncertainty on the efficiency is related to the size of the MC sample. The bin efficiencies are used to calculate the expected yield for each tag mode as given in Eqs. (10), (12), (14) and (15).

Both pseudo-flavor DT yields with $F \in (K^- \pi^+, K^- \pi^+ \pi^0)$ have contamination from DCS decays whose contribution is enhanced compared to ST yields due to the quantum correlation between the $D^0 \bar{D}^0$. Since these decays are used to determine $K_i^{(\prime)}$, the presence of this DCS contamination may bias the values [39]. In order to correct for this effect, the yield in each bin is multiplied by a correction factor estimated using the decay model reported in Ref. [16]. The correction factors f_i^F for $D^0 \rightarrow K_S^0 K^+ K^-$ against F and $f_i^{F'}$ for $D^0 \rightarrow K_L^0 K^+ K^-$ against F are given by

plitudes, for example $|\mathcal{A}(D^0 \rightarrow K^+ \pi^-)/\mathcal{A}(D^0 \rightarrow K^- \pi^+)|$

TABLE IV. Values of the parameters used to calculate the DCS correction factors.

F	r_D^F (%)	δ_D^F ($^\circ$)	R_F
$K\pi$	5.86 ± 0.02 [41]	$194.7^{+8.4}_{-17.6}$ [41]	1
$K\pi\pi^0$	4.47 ± 0.12 [42]	198^{+14}_{-15} [42]	0.81 ± 0.06 [42]

for $K^\pm\pi^\mp$, and δ_F^D is the strong-phase difference between the DCS and CF amplitudes. The coherence factor, R_F for flavor-mode F , accounts for the dilution in interference effects that arises when integrating over the phase space of multi-body decays [40]. The values of the parameters used to determine the correction factors are listed in Table IV. The fraction of events in each bin $F_i^{(\prime)}$, defined in Eq. (4), is given in Table V. The $D^0 \rightarrow K_L^0 K^+ K^-$ amplitude model is developed by modifying the intermediate resonances of $D^0 \rightarrow K_S^0 K^+ K^-$ as presented in Ref. [24]. Good agreement with the predicted values [14] is observed for the results given in Table V. The uncertainties in the final result due to the correction factors are small and are treated as a systematic uncertainty. The DCS correction is not required for the $D^0 \rightarrow K^- e^+ \nu_e$ flavor-tag.

TABLE V. Values of $F_{(-)i}$ and $F'_{(-)i}$ (%) measured from the flavor-tagged $D^0 \rightarrow K_S^0 K^+ K^-$ and $D^0 \rightarrow K_L^0 K^+ K^-$ data for the different number of bins \mathcal{N} .

i	F_i (%)	F_{-i} (%)	F'_i (%)	F'_{-i} (%)
$\mathcal{N} = 2$				
1	24.4 ± 1.7	30.4 ± 1.9	23.5 ± 1.2	27.7 ± 1.3
2	19.6 ± 1.6	25.6 ± 1.9	23.1 ± 1.3	25.6 ± 1.3
$\mathcal{N} = 3$				
1	21.9 ± 1.5	27.7 ± 1.8	21.1 ± 1.1	25.1 ± 1.2
2	21.3 ± 1.7	24.7 ± 1.8	22.6 ± 1.3	25.1 ± 1.4
3	1.3 ± 0.4	3.1 ± 0.5	2.8 ± 0.3	3.3 ± 0.4
$\mathcal{N} = 4$				
1	21.1 ± 1.5	27.0 ± 1.8	19.5 ± 1.0	23.2 ± 1.7
2	6.5 ± 0.9	3.6 ± 0.6	7.2 ± 0.7	4.1 ± 0.5
3	16.3 ± 1.5	22.4 ± 1.8	19.5 ± 1.2	23.0 ± 1.3
4	0.5 ± 0.2	2.6 ± 0.5	0.9 ± 0.2	2.6 ± 0.3

B. Bin-by-bin background estimation

In this section we explain the method used to estimate the peaking background. The amount of combinatorial background in each bin is estimated from the sideband-estimation methods described in Sec. VI B.

The peaking backgrounds are identified from the inclusive MC samples using the tool described in Ref. [43]. The backgrounds to fully reconstructed tags are found to be negligible. However, all the $D \rightarrow K_L^0 X$ modes contain backgrounds from $D \rightarrow K_S^0 X$ modes, where the π^0 mesons from $K_S^0 \rightarrow \pi^0\pi^0$ decays are not reconstructed, so that the K_S^0 is treated as a missing particle. The $D \rightarrow K_L^0 X$ and $D \rightarrow K_S^0 X$ decays are of opposite CP , hence the distribution of background events across the Dalitz plot is not the same as that

for signal events. The level of these backgrounds varies between 2 to 4% depending on the tag mode. The bin-by-bin background estimation using the inclusive MC sample is not reliable for two reasons. First, there can be a difference between the branching fraction in data and that assumed in the MC simulation. Second, the MC samples are not tuned to reflect the distributions of events across the Dalitz plot. Both these issues will result in an incorrect estimation of the bin-by-bin background. Hence, we use a combination of data and background MC samples to estimate the backgrounds.

Our method of peaking background estimation is as follows. We generate dedicated background MC samples corresponding to each type of background decay. The background retention efficiencies for these backgrounds are calculated for each bin. The expected yields are calculated using the values of c_i and s_i obtained from the previous measurement [14] through the relations given in Eqs. (10), (12), (14) and (15). The yields are multiplied by the retention efficiencies to obtain the expected background yields in data. Though most of the combinatorial background beneath the $D \rightarrow K_L^0 X$ signal decays are from non-resonant $D \rightarrow K^+ K^- \pi^0 \pi^0$ decays, these decays only contribute approximately 2% of the background in the signal region. The contributions from continuum backgrounds and low-lying charmonium resonance decays are found to be negligible for all DT modes, which is expected given the tight kinematic criteria that can be imposed close to open-charm threshold. The expected background yields are not subtracted from signal yield but added to the expected signal yield in the fit as explained in Sec. VIII.

VIII. EXTRACTION OF c_i AND s_i

The uncorrected yields in related bins are combined according to the symmetry relations described in Sec. II. This procedure reduces the number of degrees of freedom in the fit. The quantities K_i (K'_i) and c_i, s_i (c'_i, s'_i) for $D \rightarrow K_S^0 \pi^+ \pi^-$ ($D \rightarrow K_L^0 \pi^+ \pi^-$) are taken from Ref. [13]. The values of $c_i^{(\prime)}$ and $s_i^{(\prime)}$ are obtained by minimizing the negative log like-

TABLE VI. Model-predicted values of Δc_i and Δs_i along with the uncertainties $\sigma_{\Delta c_i}$ and $\sigma_{\Delta s_i}$ for equal- $\Delta\delta_D$ binnings $\mathcal{N} = 2, 3$ and 4. The values are those reported in Ref. [24].

\mathcal{N}	i	c_i	c'_i	Δc_i	s_i	s'_i	Δs_i
2	1	0.742	0.768	0.026 ± 0.017	0.275	0.286	0.011 ± 0.023
	2	-0.679	-0.680	-0.001 ± 0.036	0.318	0.397	0.079 ± 0.021
3	1	0.801	0.827	0.026 ± 0.014	0.268	0.269	0.001 ± 0.023
	2	-0.657	-0.593	0.064 ± 0.019	0.411	0.435	0.024 ± 0.010
	3	-0.043	-0.680	-0.637 ± 0.311	-0.661	0.126	0.787 ± 0.161
4	1	0.845	0.864	0.019 ± 0.011	0.239	0.242	0.003 ± 0.021
	2	-0.028	0.095	0.123 ± 0.029	0.531	0.512	-0.019 ± 0.022
	3	-0.804	0.779	0.025 ± 0.019	0.332	0.382	0.050 ± 0.015
	4	0.232	-0.718	-0.950 ± 0.355	0.738	0.262	1.000 ± 0.254

TABLE VII. Fit results for $c_i^{(l)}$ and $s_i^{(l)}$ for different \mathcal{N} . The first uncertainty is statistical and the second uncertainty is systematic.

\mathcal{N}	i	c_i	s_i	c'_i	s'_i
2	1	$0.704 \pm 0.034 \pm 0.003$	$-0.038 \pm 0.144 \pm 0.039$	$0.730 \pm 0.035 \pm 0.003$	$-0.028 \pm 0.144 \pm 0.039$
	2	$-0.760 \pm 0.040 \pm 0.007$	$0.590 \pm 0.198 \pm 0.085$	$-0.785 \pm 0.034 \pm 0.006$	$0.669 \pm 0.198 \pm 0.086$
3	1	$0.724 \pm 0.035 \pm 0.003$	$-0.037 \pm 0.174 \pm 0.049$	$0.751 \pm 0.036 \pm 0.003$	$-0.037 \pm 0.174 \pm 0.049$
	2	$-0.576 \pm 0.050 \pm 0.009$	$0.616 \pm 0.146 \pm 0.047$	$-0.512 \pm 0.050 \pm 0.009$	$0.640 \pm 0.146 \pm 0.047$
	3	$-0.174 \pm 0.173 \pm 0.040$	$-0.669 \pm 0.370 \pm 0.119$	$-0.382 \pm 0.145 \pm 0.040$	$0.045 \pm 0.384 \pm 0.116$
4	1	$0.783 \pm 0.034 \pm 0.003$	$-0.242 \pm 0.173 \pm 0.051$	$0.802 \pm 0.034 \pm 0.003$	$-0.239 \pm 0.174 \pm 0.051$
	2	$-0.053 \pm 0.106 \pm 0.017$	$0.306 \pm 0.294 \pm 0.125$	$0.070 \pm 0.106 \pm 0.017$	$0.286 \pm 0.294 \pm 0.124$
	3	$-0.654 \pm 0.057 \pm 0.011$	$0.659 \pm 0.210 \pm 0.059$	$-0.630 \pm 0.056 \pm 0.011$	$0.709 \pm 0.210 \pm 0.059$
	4	$0.090 \pm 0.208 \pm 0.041$	$-0.713 \pm 0.387 \pm 0.195$	$-0.290 \pm 0.201 \pm 0.036$	$0.122 \pm 0.422 \pm 0.206$

likelihood expression

$$\begin{aligned}
-2 \ln \mathcal{L} = & -2 \sum_i \ln P(N_i^\pm, \langle N_i^\pm \rangle)_{K_S^0 K^+ K^-, CP} \\
& -2 \sum_i \ln P(N_i^{\prime\pm}, \langle N_i^{\prime\pm} \rangle)_{K_L^0 K^+ K^-, CP} \\
& -2 \sum_{i,j} \ln P(N_{ij}, \langle N_{ij} \rangle)_{K_S^0 K^+ K^-, K_S^0 K^+ K^-} \\
& -2 \sum_{i,j} \ln P(N'_{ij}, \langle N'_{ij} \rangle)_{K_S^0 K^+ K^-, K_L^0 K^+ K^-} \\
& -2 \sum_{i,j} \ln P(N_{ij}, \langle N_{ij} \rangle)_{K_S^0 K^+ K^-, K_S^0 \pi^+ \pi^-} \\
& -2 \sum_{i,j} \ln P(N'_{ij}, \langle N'_{ij} \rangle)_{K_S^0 K^+ K^-, K_L^0 \pi^+ \pi^-} \\
& -2 \sum_{i,j} \ln P(N'_{ij}, \langle N'_{ij} \rangle)_{K_L^0 K^+ K^-, K_S^0 \pi^+ \pi^-} \\
& + \chi^2. \tag{28}
\end{aligned}$$

Here, $\langle N \rangle$ is the expected migration-corrected yield in a particular bin whose measured yield is N . $P(N, \langle N \rangle)$ is the Poisson probability of observing a yield N given the mean $\langle N \rangle$:

$$P(N, \langle N \rangle) = \frac{\langle N \rangle^N e^{-\langle N \rangle}}{N!}. \tag{29}$$

If $\langle M \rangle$ represents the expected signal yield and $\langle B \rangle$ represents the expected background then $\langle N \rangle = \langle M \rangle + \langle B \rangle$. It is

to be noted that in Eq. (28) the comparison is between the uncorrected yield and the sum of expected signal and expected background in each bin. This method eliminates the possibility of unphysical negative bin yields arising from the subtraction of backgrounds from bins having low yields. The χ^2 term in Eq. (28) constrains the difference between the extracted values of c_i (s_i) and c'_i (s'_i) to lie within the uncertainties of the predicted differences Δc_i (Δs_i). The χ^2 is defined as

$$\chi^2 = \sum_i \left(\frac{c'_i - c_i - \Delta c_i}{\sigma_{\Delta c_i}} \right)^2 + \sum_i \left(\frac{s'_i - s_i - \Delta s_i}{\sigma_{\Delta s_i}} \right)^2, \tag{30}$$

where $\Delta c_i = c'_{i, \text{BaBar}} - c_{i, \text{BaBar}}$ ($\Delta s_i = s'_{i, \text{BaBar}} - s_{i, \text{BaBar}}$) is the predicted difference from the BaBar model [16] and $\sigma_{\Delta c_i}$ ($\sigma_{\Delta s_i}$) is the uncertainty on Δc_i (Δs_i). The values of Δc_i (Δs_i) and $\sigma_{\Delta c_i}$ ($\sigma_{\Delta s_i}$) are given in Table VI.

Large values of Δc_i and Δs_i are observed in bins $i = 3$ and $i = 4$ in the $\mathcal{N} = 3$ and $\mathcal{N} = 4$ binnings, respectively. These bins correspond to the lobes on the Dalitz plot that encompass the neutral resonance $a_0(1450)^0$. The model has very small amplitudes in this region, hence a small difference between the $D \rightarrow K_S^0 K^+ K^-$ and $D \rightarrow K_L^0 K^+ K^-$ models is proportionally more significant. Consequently, the uncertainties are also large. Improvement in the precision due to the χ^2 term is more significant for s_i than c_i . The minimization of Eq. (28) is performed using the MINUIT [44] package. The value of parameters obtained from the fit are given in Table VII.

The fitting procedure is validated using pseudodata samples generated by a standalone simulation. The bin yields and backgrounds are generated according to the relations given in Sec. II. The effects of bin migration are also considered in the

simulation. The bin yields are fluctuated assuming a Poisson distribution. The procedure is repeated 500 times to obtain a pull distributions for $c_i^{(l)}$ and $s_i^{(l)}$. The means and widths of the pulls in each bin are consistent with zero and one, respectively, indicating no bias and proper estimation of the uncertainties.

IX. SYSTEMATIC UNCERTAINTIES

The evaluation of systematic uncertainties arising due to various inputs to the $c_i^{(l)}$ and $s_i^{(l)}$ fit are described in this section. In general, our method of evaluating systematic uncertainties uses a smearing procedure of the nominal input values within their uncertainties. This process is repeated 1000 times and the distribution of the resulting $c_i^{(l)}$ and $s_i^{(l)}$ values is fit with a Gaussian distribution. The width of the Gaussian distribution is then reported as the systematic uncertainty. If there is a set of correlated input quantities assumed in our fit, we use a procedure based on the Cholesky decomposition of the covariance matrix to smear the value taking the correlation into account. The procedure involves generating a vector of correlated variables $\mathbf{X} = \boldsymbol{\mu} + \mathbf{A}\mathbf{Z}$, where $\boldsymbol{\mu}$ is a vector of the reported values of the input parameter, \mathbf{Z} is a vector with random values that follow a normal distribution, and \mathbf{A} is the decomposed matrix. The fit is repeated with the new value of \mathbf{X} . The systematic covariance matrix is calculated using the distributions of the $c_i^{(l)}$ and $s_i^{(l)}$ values as well as the correlations between them.

The systematic uncertainties related to the ST yields are evaluated as follows. First, a combined systematic uncertainty in the yields due to various assumptions made in the fit is estimated. For example, the endpoints of the ARGUS function are fixed in our fits. We rerun the fits by changing the endpoints by $\pm 0.5 \text{ MeV}/c^2$, which is the approximate uncertainty related to the beam-energy spread in the endpoint. The difference between the new value of the yield and the nominal value is taken as a systematic uncertainty in the ST yield. Other assumptions include the estimation of peaking backgrounds from MC simulations and the assumed branching fractions in partially reconstructed modes. The statistical uncertainties in the yields from the fits are added in quadrature with the systematic uncertainties to obtain the total uncertainty related to the ST fit. The ST yield is smeared within the total uncertainty and the distribution of the resulting $c_i^{(l)}$ and $s_i^{(l)}$ values is obtained as laid out above. The systematic uncertainties due to the ST yield are found to be small. The systematic uncertainty due to the factors used to correct for the effect of charm mixing is found to be negligible. Furthermore, uncertainties related to the absolute efficiency do not affect the results due to the use of yield ratios and normalization constants fit to data.

The systematic uncertainty due to the finite statistics of the flavor-tag yields K_i are evaluated by smearing the input values assuming a Gaussian distribution around the nominal value with width equal to the uncertainty. The systematic uncertainty due to the flavor-tag yield of the $D \rightarrow K_{S,L}^0 \pi^+ \pi^-$ decay is estimated using the covariance matrix reported in

the Ref. [13]. The uncertainties due to flavor-tag yields are small due to the large yields compared to those for CP and $D \rightarrow K^0 h^+ h^-$ tags.

In our fit the values of $c_i^{(l)}$ and $s_i^{(l)}$ of $D \rightarrow K_{S,L}^0 \pi^+ \pi^-$ are fixed to the values reported in Ref. [13]. The covariance matrix used to smear the values is also taken from Ref. [13]. This uncertainty is the dominant systematic uncertainty.

The value of the total number of $D^0 \bar{D}^0$ pairs is fixed in our fits. This information is used to normalize the bin yields of $D \rightarrow K_{S,L}^0 K^+ K^-$ tagged by $D \rightarrow K_{S,L}^0 h^+ h^-$ decays. The related systematic uncertainty is evaluated by smearing the value of $N_{D^0 \bar{D}^0}$ within its uncertainty assuming a Gaussian distribution. Since the value of $N_{D^0 \bar{D}^0}$ pairs is measured precisely [36], the systematic uncertainty due to this input is negligible.

Signal MC samples are widely used in this analysis for various purposes such as constructing migration matrices and determining the selection efficiencies. The systematic uncertainties due to the finite size of the MC samples are evaluated by smearing the matrix elements within their uncertainties assuming a Gaussian distribution taking correlations into account. Any systematic uncertainty due to the incorrect MC modelling is cancelled since we use ratios of ST and DT yields in computing the values of $\langle M \rangle$.

The effect of bin-by-bin peaking background from $D \rightarrow K_S^0 h^+ h^-$ decays in the $D \rightarrow K_L^0 h^+ h^-$ signal sample is estimated using the c_i and s_i values reported in Ref. [14]. To estimate the systematic uncertainty from the background parametrization, the estimated amount of background is varied by a Gaussian function within its statistical uncertainty. The level of the background with respect to the partially reconstructed tags is larger than that with respect to the fully reconstructed tags, hence the systematic uncertainties due to the background parametrization for partially reconstructed tags are larger than those for the fully reconstructed tags. Since the backgrounds are only identified but not estimated from MC simulations, there is no systematic uncertainty arising due to any difference in branching fractions between data and MC simulations.

The systematic uncertainties due to the assumed values of the DCS correction factors to the flavor-tag yields $f_i^{F(l)}$ are estimated by smearing the correction factors within their uncertainties assuming a Gaussian distribution. The $f_i^{F(l)}$ uncertainties are small, hence the associated systematic uncertainties on the values of $c_i^{(l)}$ and $s_i^{(l)}$ are also small.

An example of the individual contributions to the systematic uncertainties for the $\mathcal{N} = 3$ equal- $\Delta\delta_D$ binning is shown in Table VIII; corresponding tables for the $\mathcal{N} = 2$ and 4 binning schemes are given in App. A. The systematic uncertainties are significantly smaller than statistical uncertainties for all binning schemes. Appendix B contains the statistical and systematic correlation matrices for the $\mathcal{N} = 2, 3$ and 4 binning schemes. The final results for c_i, s_i, c_i' and s_i' are shown in Fig. 8.

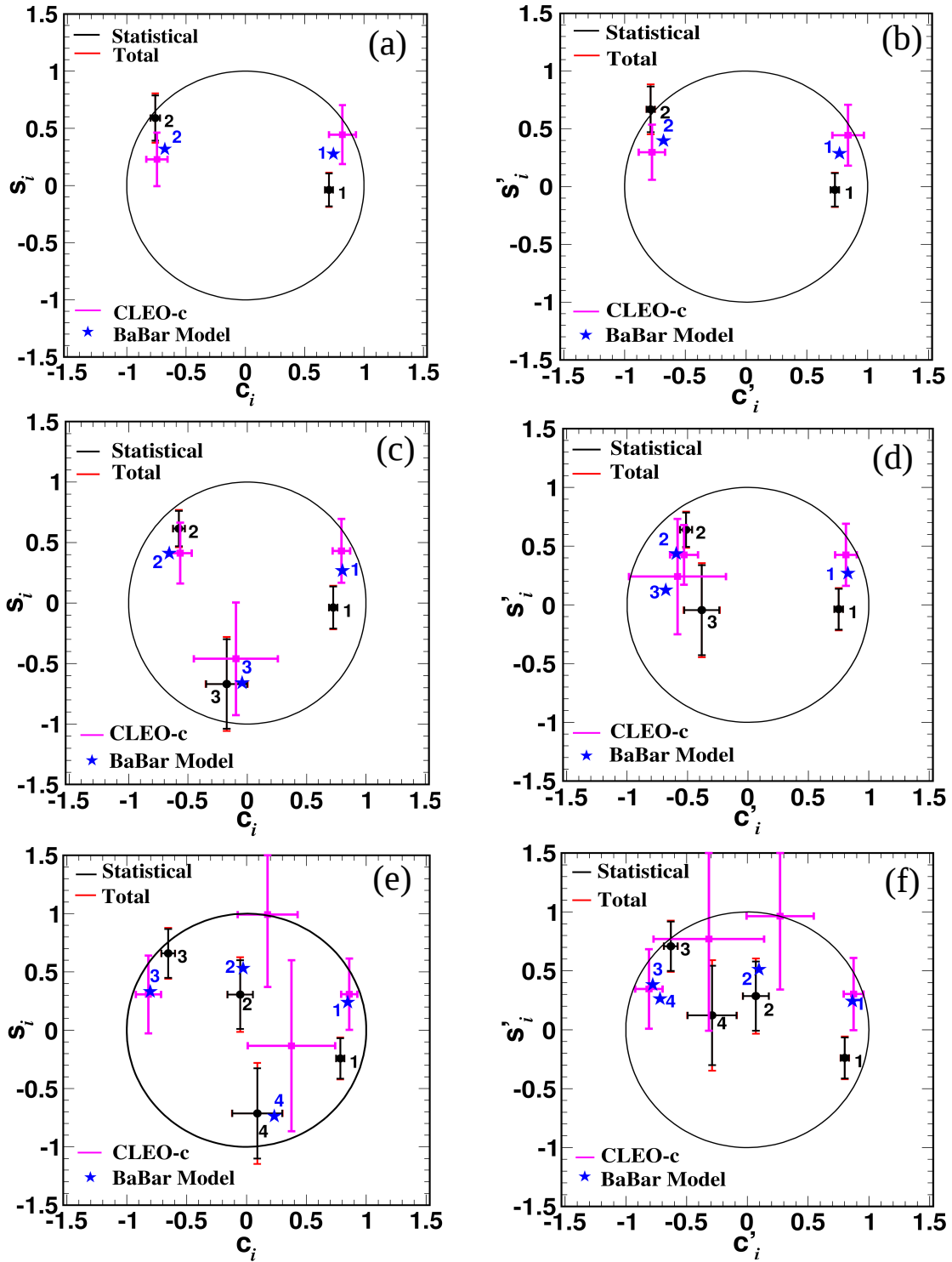


FIG. 8. Measured values of $c_i^{[l]}$ and $s_i^{[l]}$ for $\mathcal{N} = 2$ (a) [(b)], $\mathcal{N} = 3$ (c) [(d)], and $\mathcal{N} = 4$ (e) [(f)] equal- $\Delta\delta_D$ bins are given by the black points with error bars. Also shown for comparison are the measurements reported by the CLEO Collaboration [14] (pink points with error bars) and the predictions of the model reported by the BaBar Collaboration [16] (blue stars). The black circle corresponds to the allowed physical region $c_i^2 + s_i^2 = 1$.

X. IMPACT OF c_i, s_i ON MEASUREMENT OF γ

The values of c_i and s_i are used as an input to the model-independent determination of γ using the $B^- \rightarrow$

$DK^-, D \rightarrow K_S^0 K^+ K^-$ decay. The uncertainties on the measured values of c_i and s_i introduce a related systematic uncertainty on the measured value of γ , which we here esti-

TABLE VIII. Summary of the contributions to the systematic uncertainty for the $\mathcal{N} = 3$ equal- $\Delta\delta_D$ binning.

Systematic	c_1	c_2	c_3	s_1	s_2	s_3	c'_1	c'_2	c'_3	s'_1	s'_2	s'_3
ST yield	0.001	0.005	0.007	0.001	0.002	0.001	0.001	0.005	0.002	0.001	0.002	0.001
$K_i^{(\prime)}$ statistics	0.001	0.006	0.033	0.006	0.001	0.010	0.001	0.006	0.033	0.006	0.001	0.010
$K^0\pi^+\pi^-(c_i^{(\prime)}, s_i^{(\prime)})$	0.002	0.003	0.010	0.045	0.044	0.085	0.002	0.003	0.004	0.045	0.044	0.083
$K^0\pi^+\pi^-(K_i^{(\prime)})$	0.001	0.001	0.003	0.009	0.015	0.018	0.001	0.001	0.001	0.009	0.015	0.018
$N_{D\bar{D}}$	0.000	0.000	0.000	0.001	0.000	0.000	0.000	0.000	0.000	0.001	0.000	0.001
MC statistics	0.001	0.003	0.013	0.000	0.001	0.000	0.001	0.003	0.020	0.000	0.001	0.000
Background	0.001	0.002	0.012	0.015	0.009	0.082	0.001	0.002	0.008	0.015	0.009	0.079
DCS correction	0.000	0.000	0.000	0.000	0.000	0.000	0.000	0.000	0.000	0.000	0.000	0.000
Statistical	0.035	0.050	0.173	0.174	0.146	0.370	0.036	0.050	0.145	0.174	0.146	0.384
Total systematic	0.003	0.009	0.040	0.049	0.047	0.119	0.003	0.009	0.040	0.049	0.047	0.116
Total	0.035	0.058	0.178	0.181	0.154	0.389	0.036	0.051	0.150	0.181	0.154	0.401

mate through a pseudodata simulation study.

We simulate the decay rate of $B^- \rightarrow DK^-, D \rightarrow K_S^0 K^+ K^-$ within the Dalitz plot bins using the relation in Eq. (3). In the simulation, the input values of c_i, s_i, T_i and T_{-i} are set to those reported here. The values of r_B, δ_B and γ are taken to be 0.103, 136.9° and 73.5°, respectively (see Ref. [41]). In order to reduce the uncertainty due to the statistics of the B decay sample to a negligible level, the pseudodata sample size is set to 5×10^6 events. The bin yields are fluctuated according to a Poisson distribution to produce a new bin yield, N^I . The expected bin yield, N^E , is calculated using c_i and s_i values obtained by smearing the measured values by their uncertainties, assuming a Gaussian distribution and taking the correlations into account. The best fit values of r_B, δ_B and γ are extracted by minimizing $\chi^2 = \sum_i (N_i^I - N_i^E)^2 / N_i^E$. The pseudodata simulations are repeated 10000 times and the resulting γ distributions for $\mathcal{N} = 2, 3$ and 4 bins are shown in Fig. 9.

The distributions of all parameters (r_B, δ_B and γ) are found to be asymmetric. Using the root mean square (RMS) of the distribution, we estimate the uncertainties on γ to be 2.3°, 1.3° and 1.3° for the schemes with $\mathcal{N} = 2, 3$ and 4 bins, respectively. We also estimate an asymmetric uncertainty by integrating 16% of the distribution in the lower and upper tails to work out a 68% confidence level; the asymmetric uncertainties on γ are ${}^{+2.4^\circ}_{-1.8^\circ}, {}^{+1.0^\circ}_{-0.9^\circ}$ and ${}^{+0.9^\circ}_{-0.9^\circ}$ for schemes with $\mathcal{N} = 2, 3$ and 4 bins, respectively. Better sensitivity for $\mathcal{N} = 3$ and 4 compared to $\mathcal{N} = 2$ is observed. This is due to the fact that dividing the data into more bins is a better approximation of the unbinned case. The lack of improvement in sensitivity while going from $\mathcal{N} = 3$ to $\mathcal{N} = 4$ is due to the nature of the $D^0 \rightarrow K_S^0 K^+ K^-$ Dalitz plot. The dominant resonances contributing to $D^0 \rightarrow K_S^0 K^+ K^-$ are $D^0 \rightarrow K_S^0 \phi$ and $D^0 \rightarrow K_S^0 a(980)^0$, which are both located close to the $M_{K^+ K^-}^2$ kinematic limit. In a binning based on equal- $\Delta\delta_D$ regions these bins are always enclosed by a similar pair of bins and the new pair of bins always encloses a region with a low density of events, as can be seen in Fig. 1.

Biases of up to 0.7° are observed in the central values of γ for all binning schemes. A bias was reported in the previous analysis as well [14]. The bias is smaller with our measurement, but non-negligible given the size of the pseudodata

sample used. In order to investigate the source of the bias, we rerun the pseudodata experiments ignoring any pairs of c_i and s_i values that lie outside the physical region given by $c_i^2 + s_i^2 < 1$; the bias is still observed, which is due to the non-Gaussian nature of the truncated c_i and s_i distributions. Therefore, instead of removing the unphysical values the uncertainties on the c_i and s_i are artificially reduced by a factor of three; in this case no observable bias is seen in any of the extracted parameters. Hence we conclude that the bias stems from some pairs of c_i and s_i values lying outside the physical region. Therefore, future measurements with a larger $\psi(3770)$ sample [45] are likely to reduce or remove this bias.

XI. SUMMARY

Using a sample of $\psi(3770)$ data corresponding to an integrated luminosity of 2.93 fb⁻¹ collected by the BESIII detector, we report a measurement of the strong-phase difference parameters for $D \rightarrow K_{S,L}^0 K^+ K^-$ decays with the best precision to date. The results presented here are an important input to model-independent measurements of the CKM angle γ using the BPGGSZ method. These values are also essential for the model-independent determination of charm-mixing parameters and in the search for CP violation in $D^0 \rightarrow K_S^0 K^+ K^-$ decays [46]. We note that the statistical uncertainties limit the precision of our measurements. Therefore, it is desirable to collect larger $\psi(3770)$ data sets in future [45].

The major source of systematic uncertainty is due to the input strong-phase difference parameters of $D \rightarrow K_{S,L}^0 \pi^+ \pi^-$ decays [13]. Significant systematic uncertainties also arise from the background parametrization of the partially reconstructed $D \rightarrow K_L^0 X$ decay modes. Both of these uncertainties depend on the size of the charm sample available.

Good agreement with the previous measurements by the CLEO Collaboration [14] is obtained in all bins. Hence, we have performed a combination of the BESIII and CLEO results, which is reported in App. C. The predictions from the BaBar model [16] lie within one to two standard deviations from our values. We have recently reported an amplitude model and branching fraction for $D^0 \rightarrow K_S^0 K^+ K^-$ decays

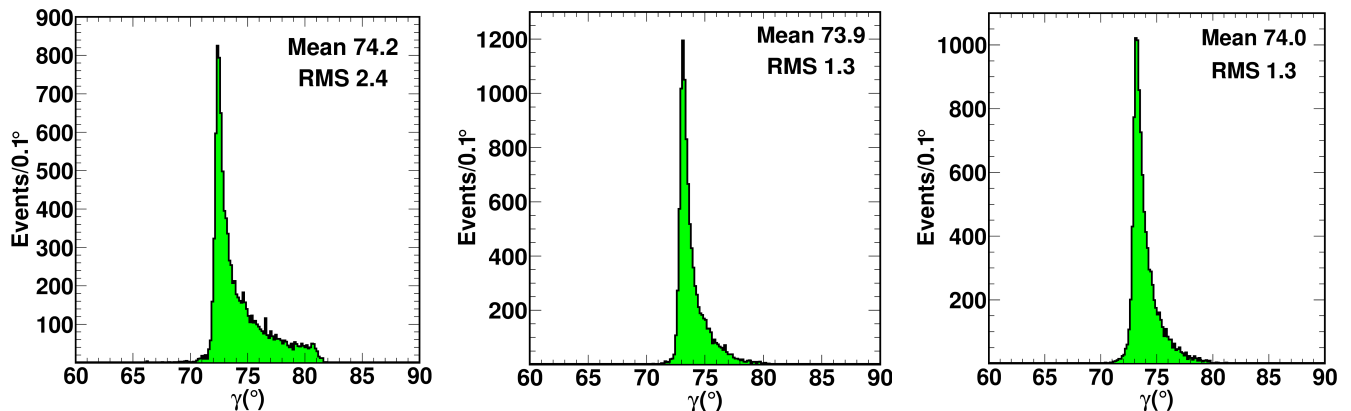


FIG. 9. Distribution of γ obtained from pseudodata experiments for $\mathcal{N} = 2$ (left), $\mathcal{N} = 3$ (middle) and $\mathcal{N} = 4$ (right) binning schemes.

[47]; the measured values of c_i and s_i are also in agreement with this model. The estimated uncertainties on γ arising from the uncertainties on the measured values of c_i and s_i are 2.3° , 1.3° and 1.3° for $\mathcal{N} = 2$, $\mathcal{N} = 3$ and $\mathcal{N} = 4$ equal- $\Delta\delta_D$ binning, respectively.

XII. ACKNOWLEDGMENTS

The BESIII Collaboration thanks the staff of BEPCII and the IHEP computing center for their strong support. This work is supported in part by National Key Basic Research Program of China under Contract No. 2015CB856700; National Natural Science Foundation of China (NSFC) under Contracts Nos. 11625523, 11635010, 11735014, 11822506, 11835012, 11935015, 11935016, 11935018, 11961141012; the Chinese Academy of Sciences (CAS) Large-Scale Scientific Facility Program; Joint Large-Scale Scientific Facility Funds of the

NSFC and CAS under Contracts Nos. U1732263, U1832207; CAS Key Research Program of Frontier Sciences under Contracts Nos. QYZDJ-SSW-SLH003, QYZDJ-SSW-SLH040; 100 Talents Program of CAS; INPAC and Shanghai Key Laboratory for Particle Physics and Cosmology; ERC under Contract No. 758462; German Research Foundation DFG under Contracts Nos. 443159800, Collaborative Research Center CRC 1044, FOR 2359, FOR 2359, GRK 214; Istituto Nazionale di Fisica Nucleare, Italy; Ministry of Development of Turkey under Contract No. DPT2006K-120470; National Science and Technology fund; Olle Engkvist Foundation under Contract No. 200-0605; STFC (United Kingdom); The Knut and Alice Wallenberg Foundation (Sweden) under Contract No. 2016.0157; The Royal Society, UK under Contracts Nos. DH140054, DH160214; The Swedish Research Council; U. S. Department of Energy under Contracts Nos. DE-FG02-05ER41374, DE-SC-0012069.

-
- [1] N. Cabibbo, Phys. Rev. Lett. **10**, 531 (1963); M. Kobayashi and T. Maskawa, Prog. Theor. Phys. **49**, 652 (1973).
 - [2] M. Gronau and D. Wyler, Phys. Lett. B **265**, 172 (1991); M. Gronau and D. London, Phys. Lett. B **253**, 483 (1991).
 - [3] J. Brod and J. Zupan, JHEP **1401**, 051 (2014).
 - [4] M. Blanke and A. J. Buras, Eur. Phys. J. C **79**, 159 (2019).
 - [5] A. Lenz and G. Tetlalmatzi-Xolocotzi, arXiv:1912.07621 [hep-ph].
 - [6] D. Atwood, I. Dunietz and A. Soni, Phys. Rev. Lett. **78**, 3257 (1997); D. Atwood, I. Dunietz and A. Soni, Phys. Rev. D **63**, 036005 (2001).
 - [7] A. Bondar, Proceedings of BINP special analysis meeting on Dalitz analysis, unpublished (2002).
 - [8] A. Giri, Y. Grossman, A. Soffer, and J. Zupan, Phys. Rev. D **68**, 054018 (2003).
 - [9] H. Aihara *et al.* (Belle Collaboration), Phys. Rev. D **85**, 112014 (2012).
 - [10] P. del Amo Sanchez *et al.* (BaBar Collaboration), Phys. Rev. Lett. **105**, 121801 (2010).
 - [11] R. Aaij *et al.* (LHCb Collaboration), J. High Energy Phys. **8**, 176 (2018).
 - [12] P.K Resmi *et al.* (Belle Collaboration), J. High Energy Phys. **10**, 178 (2019).
 - [13] M. Abilikhim *et al.* (BESIII Collaboration) Phys. Rev. Lett. **124**, 241802 (2020); Phys. Rev. D **124**, 241802, (2020).
 - [14] J. Libby *et al.* (CLEO Collaboration), Phys. Rev. D **82**, 112006 (2010).
 - [15] C. Thomas and G. Wilkinson, J. High Energy Phys. **10** 185 (2012).
 - [16] P. del Amo Sanchez *et al.* (BaBar Collaboration), Phys. Rev. D. **78**, 034023 (2008).
 - [17] M. Battaglieri *et al.*, Acta Phys. Polon. B **46** 257 (2015).
 - [18] P. del Amo Sanchez *et al.* (BaBar Collaboration), Phys. Rev. Lett. **105**, 121801 (2010).
 - [19] A. Poluektov *et al.* (Belle Collaboration), Phys. Rev. D **81**, 112002 (2010).
 - [20] R. Aaij *et al.* (LHCb Collaboration), arXiv:1808.08865 [hep-ex].
 - [21] E. Kou *et al.* (Belle II Collaboration), PTEP **2019**, no. 12, 123C01 (2019)
 - [22] A. Bondar and A. Poluektov, Eur. Phys. J. C **47**, 347 (2006); A. Bondar and A. Poluektov, Eur. Phys. J. C **55**, 51 (2008).

- [23] S. M. Flatt, Phys. Lett. B **63**, 224 (1976).
- [24] C. Thomas (D.Phil. Thesis), University of Oxford (2011), (Retrieved from <http://cds.cern.ch/record/1427272>).
- [25] M. Ablikim *et al.* (BESIII Collaboration), Chin. Phys. C **37**, 123001 (2013).
- [26] M. Ablikim *et al.* (BESIII Collaboration), Nucl. Instrum. Methods Phys. Res., Sect. A **614**, 345 (2010).
- [27] S. Agostinelli *et al.* (GEANT4 Collaboration), Nucl. Instrum. Methods Phys. Res., Sect. A **506**, 250 (2003); J. Allison *et al.*, IEEE Trans. Nucl. Sci. **53**, 270 (2006); Z. Y. Deng *et al.*, High Energy Physics and Nuclear Physics **30**, 371 (2006).
- [28] S. Jadach, B. F. L. Ward, and Z. Was, Comput. Phys. Commun. **130**, 260 (2000).
- [29] D. J. Lange, Nucl. Instrum. Meth. A **462**, 152 (2001).
- [30] P.A. Zyla *et al.* (Particle Data Group), Prog. Theor. Exp. Phys. **2020**, 083C01 (2020).
- [31] J. C. Chen *et al.*, Phys. Rev. D **62**, 034003 (2000).
- [32] E. Barberio and Z. Was, Comput. Phys. Commun. **79**, 291 (1994).
- [33] D. Ambrose (Ph.D. Thesis), University of Rochester (2014), (Retrieved from <https://inspirehep.net/literature/1669241>).
- [34] S. Malde *et al.*, Phys. Lett. B **747**, 9 (2015).
- [35] H. Albrecht *et al.* (ARGUS Collaboration), Phys. Lett. B **241**, 278 (1990).
- [36] M. Ablikim *et al.* (BESIII Collaboration), Chin. Phys. C **42**, 083001 (2018).
- [37] I.I. Bigi and H. Yamamoto, Phys. Lett. B **349**, 363 (1995).
- [38] D. M. Asner *et al.* (CLEO Collaboration), Phys. Rev. D **78**, 012001 (2008).
- [39] R. A. Briere (CLEO Collaboration), Phys. Rev. D. **80**, 032002 (2009).
- [40] D. Atwood and A. Soni, Phys. Rev. D **68**, 033003 (2003).
- [41] Y. Amhis *et al.* (Heavy Flavor Averaging Group), Eur. Phys. J. C **77**, 895 (2017); and updates at <https://hflav.web.cern.ch>
- [42] J. Libby *et al.*, Phys. Lett. B **757**, 520 (2016); Phys. Lett. B **765**, 402 (2017).
- [43] X. Zhou, S. Du, G. Li and C. Shen, arXiv:2001.04016 [hep-ex].
- [44] F. James and M. Roos, Comput. Phys. Commun. **10**, 343 (1975).
- [45] M. Ablikim *et al.* (BESIII Collaboration), Chin. Phys. C **44**, 040001 (2020).
- [46] R. Aaij *et al.* (LHCb Collaboration), Phys. Rev. Lett. **122**, 231802 (2019).
- [47] M. Ablikim *et al.* (BESIII Collaboration), arXiv:2006.02800 [hep-ex].

Appendix A: Additional tables of systematic uncertainties

The contributions to the systematic uncertainty of the $c_i^{(\prime)}$ and $s_i^{(\prime)}$ measurements for the $\mathcal{N} = 2$ and $\mathcal{N} = 4$ binning schemes are given in Tables IX and X, respectively. These tables complement Table VIII for the $\mathcal{N} = 3$ binning scheme, which is given in Sec. IX.

Appendix B: Statistical and systematic covariance matrices

We report the statistical (systematic) covariance matrices related to the measurements for the $\mathcal{N} = 2, 3$ and 4 binning schemes in Tables XI (XII), XIII (XIV) and XV (XVI), respectively.

Appendix C: Combination of BESIII and CLEO results

The results presented in this paper are compatible with those reported by the CLEO Collaboration [14]. Therefore, it is advantageous to perform an average of the two sets of results to get the best possible estimates of $c_i^{(\prime)}$ and $s_i^{(\prime)}$. Following Ref. [13], the average is calculated by adding a multi-dimensional constraint term to the log-likelihood expression given in Eq. (28). The constraint term is defined as

$$\chi_{\text{avg}}^2 = (\mathbf{P} - \mathbf{P}^{\text{CLEO}})^T \mathbf{V}^{-1} (\mathbf{P} - \mathbf{P}^{\text{CLEO}}), \quad (\text{C1})$$

where \mathbf{P} is the vector of $4\mathcal{N}$ parameters in the fit, \mathbf{P}^{CLEO} is the vector of corresponding values reported by the CLEO Collaboration and \mathbf{V} is the $4\mathcal{N} \times 4\mathcal{N}$ combined statistical and systematic covariance matrix related to the CLEO measurements. The values of $c_i^{(\prime)}$ and $s_i^{(\prime)}$ obtained from the fit including the χ_{avg}^2 term are given in Table XVII. The uncertainty returned by the fit only includes the BESIII statistical and total CLEO uncertainties. Hence, to take account of the systematic uncertainties related to the BESIII measurement, the uncertainties reported in Table XVII are the sum in quadrature of those returned by the fit and the systematic uncertainties reported in Tables VIII, IX and X. Calculating the uncertainty in this way assumes the systematic uncertainties related to the BESIII and CLEO measurements are uncorrelated; this is a valid assumption because the systematic uncertainties are dominated by those related to the strong-phase measurements of $D \rightarrow K_S^0 \pi^+ \pi^-$ used in each analysis, which are independent measurements from the respective experiments. The correlation matrices reported in Tables XVIII-XX are obtained by summing the covariance matrix from the fit with the systematic covariance matrix.

